

# Interannual Variations of Heat Budget over the Eastern Ross Sea Shelf and the Forcing Mechanisms

Yuanjie Chen (✉ [chenyuanjie@sjtu.edu.cn](mailto:chenyuanjie@sjtu.edu.cn))

Shanghai Jiao Tong University

Zhaoru Zhang

Shanghai Jiao Tong University <https://orcid.org/0000-0001-6125-8660>

Xuezhu Wang

Hohai University

Xiaohui Liu

State Key Laboratory of Satellite Ocean Environment Dynamics

Meng Zhou

Shanghai Jiao Tong University

---

## Research Article

**Keywords:** Eastern Ross Sea shelf, Heat budget, Horizontal heat advection, Circumpolar deep water intrusion, High salinity shelf water transport, Eddy activities

**Posted Date:** April 18th, 2022

**DOI:** <https://doi.org/10.21203/rs.3.rs-1551617/v1>

**License:**  This work is licensed under a Creative Commons Attribution 4.0 International License.

[Read Full License](#)

---

# Abstract

The temporal variation of heat budget in the subsurface layer of the eastern Ross Sea shelf (ERSS) is crucial for understanding the stability of ice shelves in the Ross Sea. In this study, six-year simulations from the Southern Ocean State Estimate (SOSE) are employed to analyze the interannual variations of heat budget in the subsurface layer of ERSS and the controlling mechanisms. The results reveal that the annual change in the heat content of the study region is dominated by the horizontal heat advection term, and only in one year the vertical advection and diffusion terms also play an important role. The horizontal advection term is co-affected by the intrusion of warm circumpolar deep water (CDW) onto the shelf across the northern boundary of ERSS, the transport of cold high salinity shelf water (HSSW) from the western Ross Sea shelf (WRSS), and the transport of CDW across the western boundary of ERSS. Contributions from these physical processes to the change of annual heat content vary over the years. The interannual variation of the CDW intrusion is modulated by the strength of eddy activities over the slope, and the interannual variation of heat transports related to HSSW is affected both by the extent of HSSW on the western shelf and coastal circulations that affect the eastward spreading of HSSW.

## 1 Introduction

The Ross Sea (Fig. 1) is a deep bay of the Southern Ocean that borders the Amundsen Sea near the Cape Colbeck and the marginal seas of East Antarctica at Cape Adare. The southern boundary of the Ross Sea abuts the Ross Ice Shelf (RIS), which is the largest ice shelf on the Earth with an average thickness of 370 m (Smith et al., 2012). The Ross Sea (and RIS) overlies a deep continental shelf with an average depth of  $\sim 530$  m (Smith et al., 2012), which is cut by several troughs including the Drygalski Trough, the Joides Trough, and the Glomar Challenger Trough running approximately in the northwest-southeast direction. These troughs facilitate the on-shelf intrusion of the circumpolar deep water (CDW; Klinck and Dinniman, 2010; St-Laurent et al., 2013), a relatively warm ( $\theta > 1.2^\circ\text{C}$ ) and salty water mass ( $S > 34.4$ ) (Orsi and Wiederwohl, 2009) that circulates along the Antarctic Circumpolar Current (ACC) and enters the cyclonic circulation of the Ross gyre at its eastern limb. Warm CDW upwells from deep layers to 200–300 m near the continental slope and intrudes onto the shelf. It then mixes with the shelf water and the Antarctic surface water (AASW), forming the modified Circumpolar Deep Water (mCDW) (Gordon et al., 2000; Jacobs and Giulivi, 1999; Orsi and Wiederwohl, 2009), which has temperature of  $\approx 1.5^\circ\text{C}$  to  $1.0^\circ\text{C}$  (Orsi and Wiederwohl, 2009) and is an important heat source to the continental shelf (Budillon et al., 2000; Dinniman et al., 2003).

Observations over the past few decades have shown a significant reduction in the salinity of shelf water (Budillon et al., 2011; Fusco et al., 2009) and surface salinity within the Ross gyre (Jacobs et al., 2002). Fresher surface water would increase the strength of the pycnocline (vertical density gradient), retaining heat in the subsurface layer, resulting in ocean warming at depths of  $\sim 300$  meters north of the continental shelf (Jacobs et al., 2002), which corresponds to the CDW layer. Poleward transport of warm CDW across the continental shelf is thought to supply most of the heat involved in the basal melt of several ice shelves along the coast in the Amundsen Sea (Hellmer et al., 1985; Jacobs et al., 1996;

Jenkins et al., 1997; St-Laurent et al., 2015; Wåhlin et al., 2010; Walker et al., 2007), the Bellingshausen Sea (Jenkins and Jacobs, 2008; Potter and Paren, 1985; Talbot, 1988) and around East Antarctica (Saari et al., 1987). Though there are multiple pathways for the CDW intrusion in the Ross Sea (Fig. 1a–b), the narrow eastern shelf makes it possible for mCDW to spread all the way to the RIS area resulting in a higher temperature of the eastern shelf than that of the western shelf (Fig. 1c, Orsi and Wiederwohl, 2009), which serves as a potential heat source to the ice shelf basal melting (Jacobs et al., 1985; Jacobs et al., 1979; Smethie and Jacobs, 2005). If more heat is retained in the subsurface layer north of the Ross Sea shelf due to enhanced stratification resulting from surface freshening, then the CDW intrusion would supply more heat to the shelf and cause greater basal melting of RIS. However, the RIS seems to be in near equilibrium with much less basal melting (Shepherd et al., 2010). There must be other factors offsetting the heat supply from CDW intrusion, which are not well understood up to now.

Based on an ocean–sea ice–ice shelf model driven by projected atmospheric forcing from phase 3 of the Coupled Model Inter-comparison Project (CMIP3), Dinniman et al. (2018) found that the increase in wind in the future will increase the on-shelf transport of CDW, but meanwhile will also enhance the vertical mixing on the shelf, inducing heat loss from the subsurface layers to the surface layer. The later process can offset the heat supplied by the CDW intrusion and result in little basal melting of RIS. This work revealed one factor that can work against the heating caused by the CDW intrusion and that helps to maintain a not too warm shelf. On the other hand, the Ross Sea is also an important source region of a cold water mass – the high salinity shelf water (HSSW) (Mathiot et al., 2012), which is the precursor of the Antarctic bottom water (AABW) (Budillon et al., 2011; Orsi et al., 1999) that supplies the lower limb of the global overturning circulation and ventilates the abyssal ocean. HSSW is mainly formed in the coastal polynyas resulting from brine rejection during new ice production, which is most prominent in the Terra Nova Bay (TNB) polynya (Fusco et al., 2009; Jendersie et al., 2018; Rusciano et al., 2013) and the western portion (between 170°E and 178°E) of the RIS polynya (Orsi and Wiederwohl, 2009). This water mass may also serve as a sink of heat on the shelf, and play a significant role in modulating the subsurface layer heat budget of the eastern Ross Sea shelf (ERSS). The contribution of HSSW production and transport to the heat budget of the Ross Sea shelf is rarely discussed by previous studies and thus remain poorly understood.

This work aims at revealing the dominant processes for the heat budget variations in the subsurface layer of ERSS, which would be important for us to understand the potential mechanisms modulating the stability of the RIS. In this study, six-year simulations from the Southern Ocean State Estimate (SOSE) product are employed to analyze the interannual variations of the heat budget and the controlling dynamical processes. It will be shown that the interannual variation of the ERSS heat content is mainly affected by variations of heat advection associated both with the CDW intrusion and the HSSW transport, while occasionally vertical mixing also plays a role. The manuscript is organized as follows. In section 2, the SOSE product is introduced and validated against observational data. The definition of the study area is provided, and the methods for computing the heat budget and relevant physical properties are described. In section 3, interannual variations of the heat budget terms and heat content in the subsurface layer of ERSS are presented, and the dynamical processes controlling these variations are

analyzed. In section 4, discussions are provided on the combined effects of CDW and HSSW transports on the annual heat content change of ERSS, the mechanisms for the HSSW transport and higher-frequency variability of the heat budget terms. In Section 5, we summarize the main findings and their significance in the context of climate change in the high latitudes of the Southern Hemisphere.

## 2 Reanalysis Product And Methods

### 2.1 Reanalysis Product

The reanalysis product used in this study is SOSE (Mazloff et al., 2010), which is part of the Estimating the Circulation and Climate (ECCO) consortium (Wunsch and Heimbach, 2007) and constrained by a large observational dataset in the Southern Ocean. SOSE is produced by an evolved version of the Massachusetts Institute of Technology general circulation model (MITgcm) (Marshall et al., 1997), which employs a sea ice model based on the work of Semtner (1976) for the thermodynamics (Fenty and Heimbach, 2013) and the work of Hibler and Bryan (1987) for the dynamics (Losch et al., 2010; Zhang and Hibler, 1997). The horizontal resolution of SOSE is  $1/6^\circ$ , which reaches 5 km on the continental slope and shelf regions in the Ross Sea in the zonal direction, approximately the scale of the baroclinic Rossby deformation radius in this area (Venaille et al., 2011). Observations reveal that the spatial scale of the CDW intrusion over the shelf is about 20 km wide (Kohut et al., 2013), and thus the resolution of SOSE is expected to reveal the CDW intrusion features. SOSE has 42 vertical levels of varying thickness. The assimilated observational data are derived from Argo floats, conductivity-temperature-depth (CTD) synoptic sections, instrument-mounted seal profiles from Southern Elephant Seals as Oceanographic Samplers (SEaOS), expendable bathythermograph (XBT) profiles, sea surface temperature observed by infrared and microwave radiometer, altimetric observations (Envisat, Geosat, Jason-1, and Ocean Topography Experiment (TOPEX/Poseidon), and sea ice cover observations from satellite (Mazloff et al., 2010). For this study, we used the SOSE iteration 100 solution, which covers the period of 2005–2010, and the ocean variables and heat budget terms are output as 5-day averaged fields.

### 2.2 Validation of SOSE

Previous studies have carried out validations of the SOSE iteration 100 solution against ocean and sea ice observations for the Southern Ocean as well as for the Ross Sea, and showed that this product can well reproduce the large-scale hydrographic structure, sea ice distributions, and the locations and ice production rates of coastal polynyas that are important formation sites of HSSW (Abernathey et al., 2016; Cerovečki et al., 2019). In this work, we first validated the SOSE output against hydrographic properties from the World Ocean Atlas 2018 (WOA18) climatology. A comparison of the temperature-salinity diagram from SOSE and from WOA18 in the Ross Sea is shown in Fig. 2, which reveals that the water mass distributions of SOSE are similar to those of WOA18, including the warm and salty CDW, the cold and salty HSSW, and the cold and fresh AASW. The comparison of potential temperature (referenced to 0 dbar in this study) profiles from SOSE and WOA18 averaged over the Ross Sea is provided in Fig. 3a. The profile of SOSE overall well matches that of WOA18. SOSE has a slightly deeper mixed layer than WOA18,

and the positions of the permanent pycnocline from SOSE and WOA are very close, which are approximately at 300 m. Below this depth to 650 m, there is a warm bias of SOSE compared to the WOA18 data. Figure 3b shows the comparison of salinity profiles from SOSE and WOA18 averaged over the Ross Sea. Though the surface salinity of SOSE is relatively small compared with WOA18, the profile of SOSE matches well with that of WOA18 below 200 m.

To further assess the performance of SOSE in simulating the thermal structure in the Ross Sea region, we validated the SOSE output against temperature data from SEaOS profiles falling in the period of 2005–2010. The comparison of potential temperature profiles from SEaOS and SOSE along an elephant seal trajectory (Fig. 1c) in January–December 2010 crossing the open ocean and the Ross Sea is presented in Fig. 4a. It is seen that SOSE can well capture the spatial pattern of potential temperature revealed from the SEaOS observations, though over the entire water column SOSE shows a slight cold temperature bias compared to SEaOS. The potential temperature sections of SOSE and SEaOS are shown in Fig. 4b–c. The pattern of SOSE temperature bears a close resemblance to that of SEaOS. In the subsurface layer, temperature from SOSE is lower than that from SEaOS in the open ocean, and higher than the latter on the shelf. The signs of warm CDW intrusion are observed at similar depths for SOSE and SEaOS, which are between 200 m and 600 m, and the intrusion occurs in the form of eddies. These validation results suggest that SOSE performs reasonably well in simulating the thermal structure in the study area, which indicates that it can capture the potential dynamical processes regulating the heat content variations.

The sea ice area simulated by SOSE is evaluated against the value estimated from the Advanced Microwave Scanning Radiometer for EOS (AMSR-E) product for the period 2005–2010 (Fig. 5). It is noted that while SOSE does not explicitly assimilate sea ice concentration data from satellite observations, the simulated sea ice area is fairly consistent with the observations, though there is a slight mismatch in austral summer. This implies that the assimilation of sea surface temperature data and the atmospheric forcing fields can effectively constrain the sea ice fields, which can impact the production of HSSW.

## 2.3 Methods

### 2.3.1 Area Division

In this study, the 1000-m isobath is used as the division between the open sea and the continental shelf of the Ross Sea (Fig. 1c). The eastern boundary of the Ross Sea is defined by the longitude line of 156 ° W. As Orsi and Wiederwohl (2009) showed that the intruded CDW mainly prevails over the Ross Sea shelf east of 180 ° E, resulting in higher potential temperature in this area (Fig. 1c), this longitude line is used as the western boundary of ERSS.

The profiles of potential temperature averaged over ERSS and the western Ross Sea shelf (WRSS) are shown in Fig. 6a–b, respectively. It can be seen that ERSS has a prominent thermocline both in summer and winter, which is located approximately at the depth of 328 m. In contrast, the thermocline in WRSS is quite weak, which is attributed to the strong vertical mixing and convection in the WRSS where intense katabatic winds from ice shelves and glaciers prevail this region (Bromwich et al., 1998; Chenoli et al.,

2012; Weber et al., 2016) and where HSSW is formed in the coastal polynyas (Jacobs et al., 1970; Thompson et al., 2020; Zhang et al., 2015). Below 100 m, the potential temperature of ERSS is significantly higher than that of WRSS, and is mostly above  $\approx 1.0$  °C and exceeds 0 °C below 200 m, indicating a large influence of CDW in this area. The vertical exchange of water is weak due to the presence of a permanent thermocline in the ERSS. Moreover, CDW is mainly in the subsurface layer (Fig. 4b–c), which is consistent with depths ranging from the bottom of the thermocline (328 m) to the sea floor (about 1000 m). Therefore, we divided the water column into surface and subsurface layers at the bottom of the thermocline, and the subsurface layer is regarded as the core depth layer for CDW intrusion, which is the focus of this study.

## 2.3.2 The Heat Budget Calculation

In this study, heat budget analysis is conducted to reveal the major terms and processes dominating the heat content variations in the subsurface layer of ERSS. The time-varying potential temperature is calculated as:

$$\theta_t = -u\theta_x - v\theta_y - w\theta_z + \nabla \cdot k\nabla\theta + \nabla^2 \cdot k_4\nabla^2\theta + D_{kpp} + D_i + F_{atm} + F_{ice},$$

$\checkmark$ tendency
 $\checkmark$ advection
 $\checkmark$ diffusion
 $\checkmark$ forcing

(1)

where  $\theta$  is potential temperature;  $\theta_t$  is the tendency term that represents the net change rate of  $\theta$ ;  $u$ ,  $v$ , and  $w$  are the eastward, northward, and vertical components of velocity, respectively;  $-u\theta_x - v\theta_y$  and  $-w\theta_z$  are the zonal, meridional and vertical advection terms, respectively;  $k$  and  $k_4$  are respectively the harmonic and biharmonic diffusion coefficients;  $D_{kpp}$  represents the parameterization of mixed-layer turbulence by the K-Profile Parameterization (KPP) (Large et al., 1994);  $D_i$  represents implicit diffusion in the model;  $F_{atm}$  is the ocean exchange with the atmosphere;  $F_{ice}$  is the ocean exchange with sea ice. The zonal, meridional, and vertical convection terms can be grouped into one advection term (advection). The harmonic, biharmonic, parameterized, and implicit diffusion terms can be grouped into one diffusion term (diffusion). The atmospheric and sea ice forcing terms can be grouped into one forcing term (forcing). Over the 6 years analyzed, the net mass divergence in the modeled Ross Sea area is negligible, and thus the ERSS heat budget is well approximated by integrating Equa. 1 over the volume of ERSS and multiplying it by the specific heat capacity  $C_v=3985$  J kg<sup>-1</sup> °C<sup>-1</sup> and the mean seawater density  $\rho_0=1035$  kg m<sup>-3</sup>(Rodriguez et al., 2016; Warren, 1999).

## 2.3.3 The Heat Transport Calculation

Following Warren (1999), the heat transport onto the ERSS across a lateral boundary of this region is calculated as

$$Q = c_p\rho_0 \int_{-D}^{-328} dz \int_{-L}^L u (\theta - \theta_f) d\lambda, \quad (2)$$

where  $c_p$  is seawater heat capacity under constant pressure, which is taken the same value as  $C_v$  in this study as the two parameters are very close;  $-D$  is the depth of the bottom of the subsurface;  $d\lambda$  is the unit distance along a lateral boundary, and  $-L$  and  $L$  are the starting and ending locations of the line integral;  $\theta - \theta_f$  is temperature minus a reference temperature, and here  $\theta$  is taken as the temperature from a grid point near the lateral boundary, and  $\theta_f$  is the average temperature over the ERSS.

## 2.3.4 Mean Kinetic Energy and Eddy Kinetic Energy Calculation

Following Von Storch et al. (2012), the MKE and EKE of ocean currents are estimated as follows:

$$MKE = \frac{1}{2} \rho_0 [ \overline{u^2} + \overline{v^2} ], \quad (3)$$

$$EKE = \frac{1}{2} \rho_0 [ \overline{(u - \overline{u})^2} + \overline{(v - \overline{v})^2} ], \quad (4)$$

where the over bar denotes annual average in this work.

## 2.3.5 The Calculation of Heat Transports Associated with CDW and HSSW

Neutral density ( $\gamma^n$ ) and salinity ( $S$ ) are normally used to distinguish between water masses in the Ross Sea. CDW is defined as  $28 < \gamma^n < 28.27 \text{ kg m}^{-3}$ , and HSSW is defined as  $\gamma^n > 28.27 \text{ kg m}^{-3}$  and  $S > 34.62$  (Orsi and Wiederwohl, 2009). The heat transport related to CDW or HSSW is calculated as:

$$Q = I_{i,j} \times c_p \rho_0 \int_{-D}^{-328} dz \int_{-L}^L u (\theta - \theta_f) d\lambda, \quad (5)$$

where  $I_{i,j}$  is an index used to indicate if the water at a grid point  $(i, j)$  is classified as CDW/HSSW ( $I_{i,j} = 1$ ) or not ( $I_{i,j} = 0$ ).

## 3 Results

### 3.1 The Interannual Variations of the Heat Budget

The heat budget terms are integrated over the subsurface layer of ERSS, and the time series of the integrated terms during the SOSE simulation period are shown in Fig. 7a. Heat exchange between the atmosphere and ocean cannot reach below the thermocline, and thus the forcing term in Equa. 1 is negligible. In 2005, both of the advection ( $Q_{adv}$ ) and diffusion ( $Q_{diff}$ ) terms fluctuated greatly and led to a large fluctuation in the tendency term ( $Q_{tend}$ ), and overall the temporal variation of  $Q_{tend}$  is more closely related to the variation of  $Q_{adv}$ . After 2005, the diffusion term became negligible, and the variation of  $Q_{tend}$  is dominated by the variation of  $Q_{adv}$ .  $Q_{adv}$  was always negative in 2006, and turned

to positive from 2007 to 2010.  $Q_{adv}$  is further decomposed into the horizontal advection term ( $Q_{hadv}$ ) and the vertical advection term ( $Q_{vadv}$ ), as shown in Fig. 7b. It is noted that  $Q_{vadv}$  was only significant in 2005, and in the other years this term was much smaller, and the variability of  $Q_{adv}$  was virtually dominated by the horizontal advection term.

## 3.2 Subsurface Heat Transports across the Open Boundaries of ERSS

As for most years,  $Q_{hadv}$  has been identified as the major component modulating the temporal variability of  $Q_{tend}$  we then analyzed the heat advection across all open lateral boundaries – the northern boundary ( $Q_{NB}$ ), the western boundary ( $Q_{WB}$ ) and the eastern boundary ( $Q_{EB}$ ) of ERSS (Fig. 1c), to explore the contribution of each term to the total horizontal advection and thus to the heat content of the study region. The results are shown in Fig. 8. The sum of heat advection across the three open boundaries  $Q_{OB}$  nearly matches  $Q_{hadv}$  with the coefficient of correlation between the time series of these two variables (R) being 0.92, and p-value (P) lower than 0.0001 (Fig. 8a). Compared to  $Q_{NB}$  and  $Q_{WB}$   $Q_{EB}$  is much smaller (not shown) and can be neglected. From 2005 to 2010,  $Q_{NB}$  was always positive (Fig. 8b), while  $Q_{WB}$  maintained negative (Fig. 8c).

The time-integrated values of  $Q_{hadv}$   $Q_{NB}$  and  $Q_{WB}$  over each year, which respectively denote the annual change of heat content (H) for the subsurface layer of ERSS associated with each term ( $\Delta H_{hadv}$   $\Delta H_{NB}$  and  $\Delta H_{WB}$ ) are provided in Fig. 8d. It is observed that  $\Delta H_{NB}$  contributed more to  $\Delta H_{hadv}$  in 2005. The dominant component for  $\Delta H_{hadv}$  switched to  $\Delta H_{WB}$  in 2006, and the persistent negative values of  $Q_{WB}$  (Fig. 8c) in this year resulted in the negative value of  $\Delta H_{hadv}$ . From 2007 to 2010,  $\Delta H_{NB}$  overwhelmed  $\Delta H_{WB}$  again and resulted in positive values of  $\Delta H_{hadv}$  in each year. However, the slight decrease of  $\Delta H_{hadv}$  from 2007 to 2010 was more regulated by  $\Delta H_{WB}$ . In general, the interannual variation of  $\Delta H_{hadv}$  depends on the variations of  $\Delta H_{NB}$  (heat input) and  $\Delta H_{WB}$  (heat output), though their contributions vary from year to year.

## 3.3 Physical Processes Controlling the Heat Advection across Different Boundaries

### 3.3.1 Heat Advection across the Northern Boundary and the CDW Intrusion

The subsurface water exchange across the northern boundary of ERSS controls the temporal variation of  $Q_{NB}$ . Previous studies indicated that mean flow (Morrison et al., 2020) and eddy activity (Klinck and Dinniman, 2010; St-Laurent et al., 2013) are the main ways of water exchange between the open sea and the continental shelf, while quantitative relationship between the mean or eddy circulations and cross-slope exchange were not revealed. To identify the mechanisms driving the variability of  $Q_{NB}$  and  $\Delta H_{NB}$  the annual-average MKE and EKE that are vertically integrated over the subsurface layer were calculated

and shown respectively in Fig. 9 and Fig. 10. Off the coast, high values of MKE and EKE occurred mainly in the troughs, i.e. the major pathways of CDW intrusion, which is near the Glomar Challenger Trough over ERSS. Large EKE values are also observed near the 1000-m isobath between 154°W and 166°W. The two zones, namely Zone 1 near the Glomar Challenger Trough and Zone 2 at 154–166 °W (Figs. 9a, 10a), are then chosen to study the relation among the variations of MKE, EKE, the CDW intrusion and heat advection.

The annual volume transport of CDW across the northern boundary ( $V_{CDW\_N}$ ) is computed and shown in Fig. 11a. It can be seen that the interannual variation of  $\Delta H_{NB}$  is significantly correlated with the variation of  $V_{CDW\_N}$  ( $R = 0.96$  and  $P = 0.002$ ), demonstrating that the CDW intrusion is the dominant process modulating the heat transport across the northern boundary of the ERSS in the subsurface layer. According to Equa. 5, the temperature difference between the northern boundary and the continental shelf ( $\theta - \theta_f$ ) should also contribute to  $\Delta H_{NB}$ . We find that the value of  $\theta - \theta_f$  was always positive and relatively stable (Fig. 12b), and the correlation between the interannual variations of  $\theta - \theta_f$  and  $\Delta H_{NB}$  is insignificant, suggesting that the variation of temperature gradient plays a minor role in the variation of  $\Delta H_{NB}$ .

As  $V_{CDW\_N}$  is the main component that determines  $\Delta H_{NB}$ , the summation of MKE over zone 1 (MKE1) and zone 2 (MKE2) were calculated separately to analyze their role in the CDW intrusion, and the same calculation was also performed for EKE (named as EKE1 and EKE2). The total MKE over Zone 1 and Zone 2 (MKE1 + MKE2) and the total EKE (EKE1 + EKE2) are shown in Fig. 11c, which almost represent the entire MKE and EKE on the slope. The total MKE was relatively stable and its interannual variation was not obvious. It is found that the total EKE regulates the interannual variation of CDW intrusion and controls the interannual variation of  $\Delta H_{NB}$  with a significant correlation between the total EKE and  $\Delta H_{NB}$  ( $R = 0.90$ ,  $P = 0.01$ ).

Figure 11d presents the contributions of EKE1 and EKE2 to the total EKE. EKE was mainly contributed by EKE1 from 2005 to 2007, while the contribution of EKE2 became more and more significant from 2008 to 2010. EKE reached a peak value in 2005, which is consistent with the strongest CDW intrusion in this year (Fig. 11a). In 2006, EKE became the lowest in both zones, in line with the weakest CDW intrusion. Based on the MKE and EKE patterns, and given the multi-year mean potential temperature distribution over the eastern shelf (Fig. 1c), the northern boundary is then divided into two sections, the western section (NBW) and the eastern section (NBE) at 175.25 °W (marked with a red star in Figs. 1c, 9a, 10a). The annually integrated values of heat advection across the western and eastern sections ( $\Delta H_{NBW}$  and  $\Delta H_{NBE}$ ) are shown in Fig. 11e. In 2005 and 2007,  $\Delta H_{NB}$  was mainly contributed by  $\Delta H_{NBW}$ . In 2006,  $\Delta H_{NBE}$  reached the lowest value among all years, corresponding to the weakest CDW volume transport onto ERSS. In 2008–2010, contributions from  $\Delta H_{NBE}$  to  $\Delta H_{NB}$  were significantly increased and gradually equaled those from  $\Delta H_{NBW}$ , consistent with the enhanced CDW transport. Given all years, the interannual variations of  $\Delta H_{NBW}$  and  $\Delta H_{NBE}$  are significantly correlated with the variations of EKE1 ( $R = 0.92$ ,  $P < 0.0001$ ) and EKE2 ( $R = 0.87$ ,  $P < 0.0001$ ) respectively. These results demonstrate that the eddy-

induced CDW intrusion, which occurs in relatively fixed areas, is the primary mechanism controlling the interannual variation of heat advection across the northern boundary of ERSS in the subsurface layer.

### 3.3.2 Relation of Heat Advection across the Western Boundary to the Dispersion of CDW and HSSW

In Fig. 8c, it is noted that  $\Delta H_{WB}$  dominated the variations of  $\Delta H_{hadv}$  in 2006, and was important for modulating the variations of  $\Delta H_{hadv}$  from 2007 to 2010.  $Q_{WB}$  and  $\Delta H_{WB}$  was mostly negative (Fig. 8c–d), indicating that there was either a source of cold water from the WRSS into the ERSS or warm water flowing out of the ERSS. The cold water source is possibly HSSW, which is mainly formed in the western Ross Sea in the TNB polynya (Fusco et al., 2009; Jendersie et al., 2018; Rusciano et al., 2013) and the RIS polynya (Orsi and Wiederwohl, 2009) during ice-freezing seasons. As such, heat transport associated separately with HSSW ( $\Delta H_{HSSW}$ ) and CDW ( $\Delta H_{CDW\_W}$ ) across the western boundary were calculated (Fig. 12a). In 2005,  $\Delta H_{WB}$  was mainly contributed by  $\Delta H_{CDW\_W}$  and the contribution from  $\Delta H_{HSSW}$  was negligible. In 2006, the contribution from  $\Delta H_{HSSW}$  weighed out the contribution from  $\Delta H_{CDW\_W}$  and resulted in the largest annual decrease of  $H_{WB}$  in this year. The contribution from  $\Delta H_{HSSW}$  became even more dominant in 2007. From 2008 to 2010,  $\Delta H_{WB}$  was gradually dominated by  $\Delta H_{CDW\_W}$  again. Figure 12b shows the relationship between the change of the H terms and the volume transports of CDW ( $V_{CDW\_W}$ ) and HSSW ( $V_{HSSW}$ ) across the western boundary. The interannual variations of  $\Delta H_{HSSW}$  and  $V_{HSSW}$  are significantly correlated ( $R = 0.99$ ,  $P < 0.0001$ ), and thus the heat content change related to HSSW is mainly controlled by the volume transport of HSSW. The correlation between the interannual variations of  $\Delta H_{CDW\_W}$  change and  $V_{CDW\_W}$  is insignificant ( $R = 0.23$ ,  $P = 0.66$ ). Especially over 2007 to 2010,  $V_{CDW\_W}$  decreased while  $\Delta H_{CDW\_W}$  increased, which implies that the major factor modulating the  $\Delta H_{CDW}$  change is the difference in potential temperature between the WRSS and ERSS, unlike the situation for  $\Delta H_{HSSW}$ .

## 4 Discussions

### 4.1 The Combined Effects of CDW and HSSW transports on the Heat Budget of ERSS

In Section 3, it is shown that the interannual variations of heat budget in the subsurface layer of ERSS are mainly contributed by the horizontal heat advection (Fig. 7b), particularly advection across the northern boundary associated with the CDW intrusion (Fig. 11a) and advection across the western boundary related both to the eastward transport of HSSW and westward transport of CDW (Fig. 12a). The competition among these processes determined the annual change of the heat content in the subsurface layer of ERSS.

The annual changes in heat content for different years associated with all processes are summarized in Fig. 13a, and the potential temperature distributions at 328 m over the Ross Sea in different years are

shown in Fig. 13b–g. In 2005, the CDW intrusion was mainly concentrated in the Glomar Challenger Trough (Zone 1) and Zone 2 near the 1000-m isobath (Fig. 13b), created by strong eddy activities (Fig. 10a), which resulted in the largest heat transport onto ERSS from the northern boundary among all years. About a third of heat carried by CDW intrusion was then transported to WRSS. With  $\Delta H_{HSSW}$  being small,  $\Delta H_{hadv}$  was dominated by the CDW intrusion and transport processes. In this year, the vertical advection and diffusion (Fig. 7a–b) terms were also important to regulate the heat budget, and the heat content change associated with these terms exceeded  $\Delta H_{hadv}$  resulting in a negative annual change of the total H. The case in 2005 is similar to that found in Dinniman et al. (2018) where vertical diffusion plays a significant role in modulating the subsurface heat content. Vertical advection and diffusion were both small in the other years, when the horizontal advection terms played a dominant role in the heat content change. In 2006, the CDW intrusion was the weakest among the six years, following a weakening in the eddy activity (Fig. 11c). This resulted in the lowest  $\Delta H_{NB}$ . The eastward transport of HSSW via the western boundary reached its peak, leading to the largest magnitude of  $\Delta H_{HSSW}$ . Together with the relatively large  $\Delta H_{CDW\_W}$ ,  $\Delta H_{WB}$  reached a maximum among all years, which resulted in significant negative values of  $\Delta H_{hadv}$  and  $\Delta H$ , and thus low potential temperature over the ERSS that were special in the period of 2005–2010 (Fig. 13c). In 2007, the CDW intrusion from the northern boundary and the eastward transport of HSSW across the western boundary were both strong, while the  $\Delta H_{CDW\_W}$  was the weakest. The dominance of CDW led to the positive values of  $\Delta H_{hadv}$  and  $\Delta H$  in this year. From 2008 to 2010, the CDW intrusion onto ERSS maintained strong, and  $\Delta H$  associated with the eastward transport of HSSW was weak; the interannual variation of  $\Delta H$  associated with the CDW transport across the western boundary closely followed the variation of  $\Delta H_{NB}$ . Overall, from 2007 to 2010, heat transport related to strong CDW intrusion across the northern boundary overwhelmed the other processes, resulting in positive annual change of heat content (Fig. 13a) and high potential temperature in the subsurface layer of ERSS. Warm water gradually extended toward the coast and west, and the ERSS was prevailed by CDW by 2010 (Fig. 13d–g). From 2008 to 2010, HSSW had little effect on offsetting the heat supply from CDW intrusion. Heat in the subsurface layer of ERSS continued to increase, as the proportion of CDW in the total volume of ERSS subsurface water increased from 72–83%, and the annual average potential temperature increased from 0.48°C to 0.80°C.

## 4.2 The Mechanism for the HSSW Transport

As shown above, the movement of HSSW is an important factor regulating the heat content change in the subsurface layer of ERSS and the interannual variation of  $\Delta H_{HSSW}$  is mainly controlled by the variation of  $V_{HSSW}$  (Fig. 12b). In particular, large amounts of HSSW were transported from WRSS to ERSS in 2006 and 2007, resulting in a significant decrease in  $\Delta H_{WB}$  and finally led to a considerable decrease in the total heat content of the subsurface ERSS in 2006 (Fig. 13a). To find out the controlling processes for the temporal variation of the HSSW volume transport, the horizontal distributions of annual-average volume of HSSW and annual-average vertical-mean flows in the subsurface layer are analyzed and presented in Fig. 14. It is seen that HSSW is mainly distributed in the western Ross Sea, particularly around the TNB Polynya, the western part of the RIS Polynya, and the troughs connecting these areas to the slope. In

2005–2007, HSSW prevailed most of the western shelf. It is noted that an anticyclonic circulation existed around the Ross Bank in 2006 and 2007, and the southern branch of this circulation facilitated the eastward spread of HSSW into ERSS, leading to the large volume transports in these two years. In 2005, though the HSSW volume on the western shelf was the largest among all years, coastal currents near the RIS were westward, inhibiting the eastward spreading of HSSW and resulting in a low contribution of  $\Delta H_{HSSW}$  to  $\Delta H_{WB}$ . From 2008 to 2010, the coverage of the HSSW over the western shelf decreased significantly and reached the minima in 2010. As a consequence, the eastward transport of HSSW was also reduced significantly, resulting in low  $\Delta H_{HSSW}$  (Fig. 13a).

## 4.3 High-Frequency Variability of the Heat Budget and the Controlling Processes

From the time series of the 5-day-average  $Q_{NB}$  and  $Q_{WB}$  shown in Fig. 8b–c, it is noted that the relative contribution of each advection term to the high-frequency (5-day) variability of  $Q_{hadv}$  for each year is occasionally different from the situation for the annual heat content change. In 2005, the variation of  $Q_{NB}$  dominated the high-frequency variation of  $Q_{hadv}$  with the correlation between their time series being 0.87 ( $P < 0.0001$ ), which is higher than the correlation between  $Q_{WB}$  and the latter ( $R = 0.64$ ,  $P < 0.0001$ ). In 2006, the dominant component for the  $Q_{hadv}$  variation changed to  $Q_{WB}$  with the correlation between their time series reaching 0.92 ( $P < 0.0001$ ), which is much higher than the correlation between  $Q_{hadv}$  and  $Q_{NB}$  ( $R = 0.54$ ,  $P < 0.0001$ ). For these two years, the dominant contributions to the high-frequency variation of  $Q_{hadv}$  and to the annual change in  $H_{hadv}$  come from the same term. Nevertheless, in 2007–2010, while the high-frequency variation of  $Q_{hadv}$  is both significantly correlated with variations from  $Q_{NB}$  and  $Q_{WB}$ ,  $Q_{WB}$  played a more important role in modulating the variability ( $R = 0.85$ ,  $P < 0.0001$ ) compared to  $Q_{NB}$  ( $R = 0.62$ ,  $P < 0.0001$ ).

For the heat advection across the northern boundary  $Q_{NB}$ , its high-frequency variability was dominated by the variability of  $Q_{NBW}$  ( $R = 0.90$ ,  $P < 0.0001$ ) in 2005, while  $Q_{NB}$  was much more correlated with the variability of  $Q_{NBE}$  from 2006 to 2010 ( $R = 0.83$  v.s.  $R = 0.55$ , Fig. 15a). To find the mechanisms for the high-frequency variability of  $Q_{NBW}$  and  $Q_{NBE}$  during the different periods, the wind stress curl ( $curl\tau$ ) over these regions was examined, which can potentially affect the CDW intrusion by modulating the upwelling of CDW at the slope (St-Laurent et al., 2013).  $curl\tau$  is computed for areas offshore of the 1000-m isobath in Zone 1 and Zone 2, i.e. the area where CDW upwelling exists. For each zone,  $curl\tau$  is first spatially averaged, and then the anomaly value is derived by subtracting the time-mean (over 2005 for Zone 1 and over 2006–2010 for Zone 2) value from the area-averaged value. In 2005 when the CDW intrusion was most prominent on the western section (Fig. 11e), the anomaly of  $Q_{NBW}$  was significantly and negatively correlated with the anomaly of  $curl\tau$  of Zone 1 ( $R = -0.61$ ,  $P < 0.0001$ ; Fig. 15b). Especially in austral winter, the minima of  $curl\tau$  anomaly corresponded to the maxima of heat advection anomaly. This indicates that the stronger negative  $curl\tau$  enhanced CDW upwelling by generating a positive (upward) anomaly of Ekman pumping velocity, which could favor the CDW onshore intrusion. Over 2006–

2010, the anomaly of  $Q_{NBE}$  was significantly and negatively correlated with anomaly of  $curl\tau$  of Zone 2 ( $R=-0.53$ ,  $P < 0.0001$ ; Fig. 15c). Therefore, wind stress curl regulates the high-frequency variability of the heat budget and EKE regulates the interannual variability of the heat budget in the ERSS. As such, when investigating the variability of heat budget of ERSS, time scales should be distinguished.

#### 4.4 The Potential Change in the Future Heat Content of the ERSS Subsurface Layer under the combined effects of CDW and HSSW transports

A long-term freshening trend has been found in the Ross Sea associated with enhanced fresh water transport from the Amundsen Sea resulting from ice shelf melting (Budillon et al., 2011; Jacobs, 2004; Nakayama et al., 2014), though such trend is suggested to show a reversal in recent years (Castagno et al., 2019). The freshening will strengthen the surface stratification on the Ross Sea shelf and retain more heat in the subsurface layer supplied by the CDW intrusion. On the other hand, the increased stability of water can reduce convection and thus the formation of cold HSSW. If the freshening trend continues in the future, these two processes mentioned above will both contribute to warmer subsurface layer of the ERSS, which may impose significant threat to the stability of the RIS. It needs to be noted again that the model employed by SOSE does not include ice shelf, and as such the influence of heat content change of ERSS on the RIS stability cannot be directly revealed, but can be inferred from the results of this study. On the other hand, Dinniman et al. (2018) suggested that under future change of wind in the Southern Ocean, which tend to strengthen over the Ross Sea area, the on-shelf CDW intrusion onto the Ross Sea shelf will be inhibited and the vertical mixing of CDW on the shelf into the surface layer will be promoted. These processes would then reduce the heat in the ERSS subsurface layer. When estimating the future change of heat in the study area, all of the above processes must be considered together. However, in our study, vertical mixing is only found to play a significant role in the ERSS subsurface heat budget in one year (2005), and it is the combined effects of CDW intrusion and HSSW formation/transports that play the most important roles in the other years. We therefore suggest that the processes affecting the future change in the transports of these two water masses should be given more attentions when evaluating the Ross Sea subsurface heat change and the ice shelf stability.

## 5 Conclusions

In this study, six-year simulations from SOSE were employed to study the interannual variations of heat budget in the subsurface layer of the ERSS. The annual changes of heat content in the study area in different years are addressed. It is found that over most years, horizontal advection was the major component modulating the interannual variation of heat content change of the ERSS, which is in turn associated with the heat transports from the northern and western boundaries of ERSS. The annual changes in heat content are the combined effects of the on-shelf CDW intrusion across the northern boundary, the transport of cold HSSW from the western shelf into the ERSS, and the transport of CDW out of the western boundary of ERSS. The relative contributions of these processes to the heat content change are quantified in this work. It is found that the former two processes play a major role in determining the annual heat content change in different time periods, and only in one year the vertical

mixing is also found to be important in the heat budget. In the future, climatic change in the high latitudes of the Southern Hemisphere, such as the shift toward the positive phase of the Southern Annular Mode (SAM) will bring changes in the wind patterns and eddy activities (Dinniman et al., 2018; Screen et al., 2009; Smith et al., 2014; Zhang et al., 2018) in the Southern Ocean, and freshening of the surface Ross Sea may continue or reverse. These will lead to changes in the CDW on-shelf intrusion, sea ice production in the coastal polynyas and thus formation of HSSW, and vertical mixing on the Ross Sea shelf. The ultimate change in the subsurface heat content of ERSS under these processes deserves exploration, and our study suggests that the change on the CDW intrusion and HSSW formation/transport should be given more emphasis for understanding the potential change in the Ross Ice Shelf stability.

## Declarations

## Acknowledgements

This work was funded by the National Natural Science Foundation of China (Grant No. 41876221 and 41941008), the Shanghai Science and Technology Committee (Grant No. 20230711100 and Grant No. 21QA1404300), the Impact and Response of Antarctic Seas to Climate Change (Grant 583 No: IRASCC 1-02-01B), the National Key Research and Development Program of China (Grant No. 2019YFC1509102) and the Advanced Polar Science Institute of Shanghai (APSYS). The SOSE solution for years 2005–2010, denoted iteration 100, is available from [sose.ucsd.edu](http://sose.ucsd.edu). The marine mammal data were collected and made publicly available by the International MEOP Consortium and the national programs that contribute to it (<http://www.meop.net>). We gratefully acknowledge the data provided by the sources mentioned above. The authors would like to thank Matthew R. Mazloff for his guidance on the SOSE data.

## References

1. Abernathy RP, Cerovecki I, Holland PR, Newsom E, Mazloff M, Talley LD (2016), Water-mass transformation by sea ice in the upper branch of the Southern Ocean overturning, *Nat Geosci*, 9(8), 596-601. <https://doi.org/10.1038/ngeo2749>.
2. Bromwich D, Liu Z, Woert AN (1998), Winter Atmospheric Forcing of the Ross Sea Polynya, *J Geophys Res-Oceans*, 75. <https://doi.org/10.1029/AR075p0101>.
3. Budillon G, Castagno P, Aliani S, Spezie G, Padman L (2011), Thermohaline variability and Antarctic bottom water formation at the Ross Sea shelf break, *Deep-Sea Res I: Oceanogr Res Pap*, 58(10), 1002-1018. <https://doi.org/10.1016/j.dsr.2011.07.002>.
4. Budillon G, Fusco G, Spezie G (2000), A study of surface heat fluxes in the Ross Sea (Antarctica), *Antarct Sci*, 12(2), 243-254. <https://doi.org/10.1017/S0954102000000298>.
5. Castagno P, et al. (2019), Rebound of shelf water salinity in the Ross Sea, *Nat Commun*, 10, 5441. <https://doi.org/10.1038/s41467-019-13083-8>.
6. Cerovečki I, Meijers AJS, Mazloff MR, Gille ST, Tamsitt VM, Holland PR (2019), The Effects of Enhanced Sea Ice Export from the Ross Sea on Recent Cooling and Freshening of the Southeast

- Pacific, *J Clim*, 32(7), 2013-2035. <https://doi.org/10.1175/JCLI-D-18-0205.1>.
7. Chenoli S, Turner J, Abu samah A (2012), A climatology of strong wind events at McMurdo station, Antarctica, *Int J Climatol*, 33, 2667-2681. <https://doi.org/10.1002/joc.3617>.
  8. Dinniman M, Klinck J, Hofmann E, Smith W (2018), Effects of Projected Changes in Wind, Atmospheric Temperature, and Freshwater Inflow on the Ross Sea, *J Clim*, 31(4), 1619–1635. <https://doi.org/10.1175/JCLI-D-17-0351.1>.
  9. Dinniman M, Klinck J, Smith W (2003), Cross-shelf exchange in a model of Ross Sea circulation and biogeochemistry, *Deep-Sea Res II: Top Stud Oceanogr*, 50(22–26), 3103-3120. <https://doi.org/10.1016/j.dsr2.2003.07.011>.
  10. Fenty I, Heimbach P (2013), Coupled Sea Ice-Ocean-State Estimation in the Labrador Sea and Baffin Bay, *J Phys Oceanogr*, 43(5), 884-904. <https://doi.org/10.1175/JPO-D-12-065.1>.
  11. Fusco G, Budillon G, Spezie G (2009), Surface heat fluxes and thermohaline variability in the Ross Sea and in Terra Nova Bay polynya, *Cont Shelf Res*, 29(15), 1887–1895. <https://doi.org/10.1016/j.csr.2009.07.006>.
  12. Gordon LI, Codispoti LA, Jennings JC, Millero F, Morrison J, Sweeney C (2000), Seasonal evolution of hydrographic properties in the Ross Sea, Antarctica, 1996–1997, *Deep-Sea Res II: Top Stud Oceanogr*, 47(15–16), 3095-3117. [https://doi.org/10.1016/S0967-0645\(00\)00060-6](https://doi.org/10.1016/S0967-0645(00)00060-6).
  13. Hellmer H, Jacobs S, Jenkins A (1985), Oceanic Erosion of a Floating Antarctic Glacier in the Amundsen Sea, *Ocean, Ice, and Atmosphere: Interactions at the Antarctic continental margin*, 75, 83-99. <https://doi.org/10.1029/AR075p0083>.
  14. Hibler WD, Bryan K (1987), A Diagnostic Ice–Ocean Model, *J Phys Oceanogr*, 17(7), 987-1015. [https://doi.org/10.1175/1520-0485\(1987\)0172.0.CO;2](https://doi.org/10.1175/1520-0485(1987)0172.0.CO;2).
  15. Jacobs SS (2004), Bottom water production and its link with the thermohaline circulation, *Antarct Sci*, 16, 427-437. <https://doi.org/10.1017/S095410200400224X>.
  16. Jacobs SS, Amos AF, Bruchhausen PM (1970), Ross Sea oceanography and Antarctic Bottom Water formation, *Deep Sea Research and Oceanographic Abstracts*, 17(6), 935-962. [https://doi.org/10.1016/0011-7471\(70\)90046-X](https://doi.org/10.1016/0011-7471(70)90046-X).
  17. Jacobs SS, Fairbanks RG, Horibe Y (1985), Origin and Evolution of Water Masses Near the Antarctic continental Margin: Evidence from H218O/H216O Ratios in Seawater, *Oceanology of the Antarctic Continental Shelf*, 59-85. <https://doi.org/10.1029/AR043p0059>.
  18. Jacobs SS, Giulivi CF (1999), Thermohaline Data and Ocean Circulation on the Ross Sea Continental Shelf, Springer Milan, Milano, pp 3-16. [https://doi.org/10.1007/978-88-470-2250-8\\_1](https://doi.org/10.1007/978-88-470-2250-8_1).
  19. Jacobs SS, Gordon AL, Ardai JL (1979), Circulation and Melting Beneath the Ross Ice Shelf, *Science*, 203, 439. <https://doi.org/10.1126/science.203.4379.439>.
  20. Jacobs SS, Hellmer HH, Jenkins A (1996), Antarctic Ice Sheet melting in the southeast Pacific, *Geophys Res Lett*, 23(9), 957-960. <https://doi.org/10.1029/96GL00723>.

21. Jendersie S, Williams MJM, Langhorne PJ, Robertson R (2018), The Density-Driven Winter Intensification of the Ross Sea Circulation, *J Geophys Res-Oceans*, 123(11), 7702– 7724. <https://doi.org/10.1029/2018JC013965>.
22. Jenkins A, Jacobs SS (2008), Circulation and melting beneath George VI Ice Shelf, Antarctica, *J Geophys Res-Oceans*, 113(C4). <https://doi.org/10.1029/2007JC004449>.
23. Jenkins A, Vaughan DG, Jacobs SS, Hellmer HH, Keys JR (1997), Glaciological and oceanographic evidence of high melt rates beneath Pine Island Glacier, West Antarctica, *J Glaciol*, 43(143), 114-121. <https://doi.org/10.3189/s0022143000002872>.
24. Klinck JM, Dinniman MS (2010), Exchange across the shelf break at high southern latitudes, *Ocean Sci*, 6(2), 513– 524. <https://doi.org/10.5194/os-6-513-2010>.
25. Kohut J, Hunter E, Huber B (2013), Small-scale variability of the cross-shelf flow over the outer shelf of the Ross Sea, *J Geophys Res-Oceans*, 118, 1863-1876. <https://doi.org/10.1002/jgrc.20090>.
26. Large WG, McWilliams JC, Doney SC (1994), Oceanic vertical mixing: A review and a model with a nonlocal boundary layer parameterization, *Rev Geophys*, 32(4), 363-403. <https://doi.org/10.1029/94RG01872>.
27. Losch M, Menemenlis D, Campin J-M, Heimbach P, Hill C (2010), On the formulation of sea-ice models. Part 1: Effects of different solver implementations and parameterizations, *Ocean Model*, 33(1), 129-144. <https://doi.org/10.1016/j.ocemod.2009.12.008>.
28. Marshall J, Adcroft A, Hill C, Perelman L, Heisey C (1997), A finite-volume, incompressible Navier Stokes model for studies of the ocean on parallel computers, *J Geophys Res-Oceans*, 102(C3), 5753-5766. <https://doi.org/10.1029/96JC02775>.
29. Mathiot P, Jourdain NC, Barnier B, Gallée H, Molines JM, Le Sommer J, Penduff T (2012), Sensitivity of coastal polynyas and high-salinity shelf water production in the Ross Sea, Antarctica, to the atmospheric forcing, *Ocean Dyn*, 62, 701-723. <https://doi.org/10.1007/s10236-012-0531-y>.
30. Mazloff MR, Heimbach P, Wunsch C (2010), An Eddy-Permitting Southern Ocean State Estimate, *J Phys Oceanogr*, 40(5), 880-899. <https://doi.org/10.1175/2009JPO4236.1>.
31. Morrison A, Hogg A, England M, Spence P (2020), Warm Circumpolar Deep Water transport toward Antarctica driven by local dense water export in canyons, *Sci Adv*, 6, eaav2516. <https://doi.org/10.1126/sciadv.aav2516>.
32. Nakayama Y, Timmermann R, Schröder M, Hellmer H (2014), On the difficulty of modeling Circumpolar Deep Water intrusions onto the Amundsen Sea continental shelf, *Ocean Model*, 84, 26-34. <https://doi.org/10.1016/j.ocemod.2014.09.007>.
33. Orsi AH, Johnson GC, Bullister JL (1999), Circulation, mixing, and production of Antarctic Bottom Water, *Prog Oceanogr*, 43(1), 55-109. [https://doi.org/10.1016/S0079-6611\(99\)00004-X](https://doi.org/10.1016/S0079-6611(99)00004-X).
34. Orsi AH, Wiederwohl CL (2009), A recount of Ross Sea water, *Deep-Sea Res II: Top Stud Oceanogr*, 56(13), 778-795. <https://doi.org/10.1016/j.dsr2.2008.10.033>.
35. Potter JR, Paren JG (1985), Interaction Between Ice Shelf and Ocean in George VI Sound, Antarctica, *Oceanology of the Antarctic Continental Shelf*, *Oceanology of the Antarctic Continental Shelf*, 43, 35-

58. <https://doi.org/10.1029/AR043p0035>.
36. Rodriguez AR, Mazloff MR, Gille ST (2016), An oceanic heat transport pathway to the Amundsen Sea Embayment, *J Geophys Res-Oceans*, 121(5), 3337– 3349. <https://doi.org/10.1002/2015JC011402>.
37. Rusciano E, Budillon G, Fusco G, Spezie G (2013), Evidence of atmosphere–sea ice–ocean coupling in the Terra Nova Bay polynya (Ross Sea–Antarctica), *Cont Shelf Res*, 61–62, 112–124. <https://doi.org/10.1016/j.csr.2013.04.002>.
38. Saari MR, Yuen DA, Schubert G (1987), Climatic warming and basal melting of large ice sheets Possible implications for East Antarctica, *Geophys Res Lett*, 14(1), 33-36. <https://doi.org/10.1029/GL014i001p00033>.
39. Screen JA, Gillett NP, Stevens DP, Marshall GJ, Roscoe HK (2009), The Role of Eddies in the Southern Ocean Temperature Response to the Southern Annular Mode, *J Clim*, 22(3), 806-818. <https://doi.org/10.1175/2008JCLI2416.1>.
40. Semtner AJ (1976), A model for the thermodynamic growth of sea ice in numerical investigation of climate, *J Phys Oceanogr*, 6(3), 379-389.
41. Shepherd A, Wingham D, Wallis D, Giles K, Laxon S, Sundal AV (2010), Correction to “Recent loss of floating ice and the consequent sea level contribution”, *Geophys Res Lett*, 37(13). <https://doi.org/10.1029/2010GL042496>.
42. Smethie WM, Jacobs SS (2005), Circulation and melting under the Ross Ice Shelf: Estimates from evolving CFC, salinity and temperature fields in the Ross Sea, *Deep-Sea Res I: Oceanogr Res Pap*, 52(6), 959-978. <https://doi.org/10.1016/j.dsr.2004.11.016>.
43. Smith W, Dinniman MS, Hofmann EE, Klinck JM (2014), The effects of changing winds and temperatures on the oceanography of the Ross Sea in the 21st century, *Geophys Res Lett*, 41(5), 1624-1631. <https://doi.org/10.1002/2014GL059311>.
44. Smith W, Sedwick P, Arrigo K, Ainley D, Orsi A (2012), The Ross Sea in a Sea of Change, *Oceanography*, 25(3), 90-103. <https://doi.org/10.5670/oceanog.2012.80>.
45. St-Laurent P, Klinck JM, Dinniman MS (2013), On the Role of Coastal Troughs in the Circulation of Warm Circumpolar Deep Water on Antarctic Shelves, *J Phys Oceanogr*, 43(1), 51-64. <https://doi.org/10.1175/JPO-D-11-0237.1>.
46. St-Laurent P, Klinck JM, Dinniman MS (2015), Impact of local winter cooling on the melt of Pine Island Glacier, Antarctica, *J Geophys Res-Oceans*, 120(10), 6718-6732. <https://doi.org/10.1002/2015JC010709>.
47. Talbot M (1988), Oceanic Environment of George VI Ice Shelf, Antarctic Peninsula, *Ann Glaciol*, 11, 161-164. <https://doi.org/10.3189/s0260305500006480>.
48. Thompson L, Smith M, Thomson J, Stammerjohn S, Ackley S, Loose B (2020), Frazil ice growth and production during katabatic wind events in the Ross Sea, Antarctica, *The Cryosphere*, 14(10), 3329-3347. <https://doi.org/10.5194/tc-14-3329-2020>.
49. Venaille A, Vallis GK, Smith KS (2011), Baroclinic Turbulence in the Ocean: Analysis with Primitive Equation and Quasigeostrophic Simulations, *J Phys Oceanogr*, 41(9), 1605-1623.

<https://doi.org/10.1175/JPO-D-10-05021.1>.

50. Von Storch J-S, et al. (2012), An estimate of the Lorenz energy cycle for the World Ocean based on the 1/10°STORM/NCEP simulation, *J Phys Oceanogr*, 42(12), 2185-2205.  
<https://doi.org/10.1175/JPO-D-12-079.1>.
51. Wåhlin AK, Yuan X, Björk G, Nohr C (2010), Inflow of Warm Circumpolar Deep Water in the Central Amundsen Shelf, *J Phys Oceanogr*, 40(6), 1427-1434. <https://doi.org/10.1175/2010JPO4431.1>.
52. Walker DP, Brandon MA, Jenkins A, Allen JT, Dowdeswell JA, Evans J (2007), Oceanic heat transport onto the Amundsen Sea shelf through a submarine glacial trough, *Geophys Res Lett*, 34(2).  
<https://doi.org/10.1029/2006GL028154>.
53. Warren B (1999), Approximating the energy transport across oceanic sections, *J Geophys Res-Oceans*, 104(C4), 7915-7919. <https://doi.org/10.1029/1998JC900089>.
54. Weber N, Lazzara M, Keller L, Cassano J (2016), The Extreme Wind Events in the Ross Island Region of Antarctica, *Weather Forecast*, 31(3), 985-1000. <https://doi.org/10.1175/WAF-D-15-0125.1>.
55. Wunsch C, Heimbach P (2007), Practical global oceanic state estimation, *Physica D: Nonlinear Phenomena*, 230(1-2), 197-208. <https://doi.org/10.1016/j.physd.2006.09.040>.
56. Zhang J, Hibler W (1997), On an efficient numerical method for modeling sea ice dynamics, *J Geophys Res-Oceans*, 102(C4), 8691-8702. <https://doi.org/10.1029/96JC03744>.
57. Zhang Z, Uotila P, Stössel A, Vihma T, Liu H, Zhong Y (2018), Seasonal southern hemisphere multi-variable reflection of the southern annular mode in atmosphere and ocean reanalyses, *Clim Dyn*, 50(3), 1451-1470. <https://doi.org/10.1007/s00382-017-3698-6>.
58. Zhang Z, Vihma T, Stoessel A, Uotila P (2015), The role of wind forcing from operational analyses for the model representation of Antarctic coastal sea ice, *Ocean Model*, 94(94), 95-111.  
<https://doi.org/10.1016/j.ocemod.2015.07.019>.

## Figures

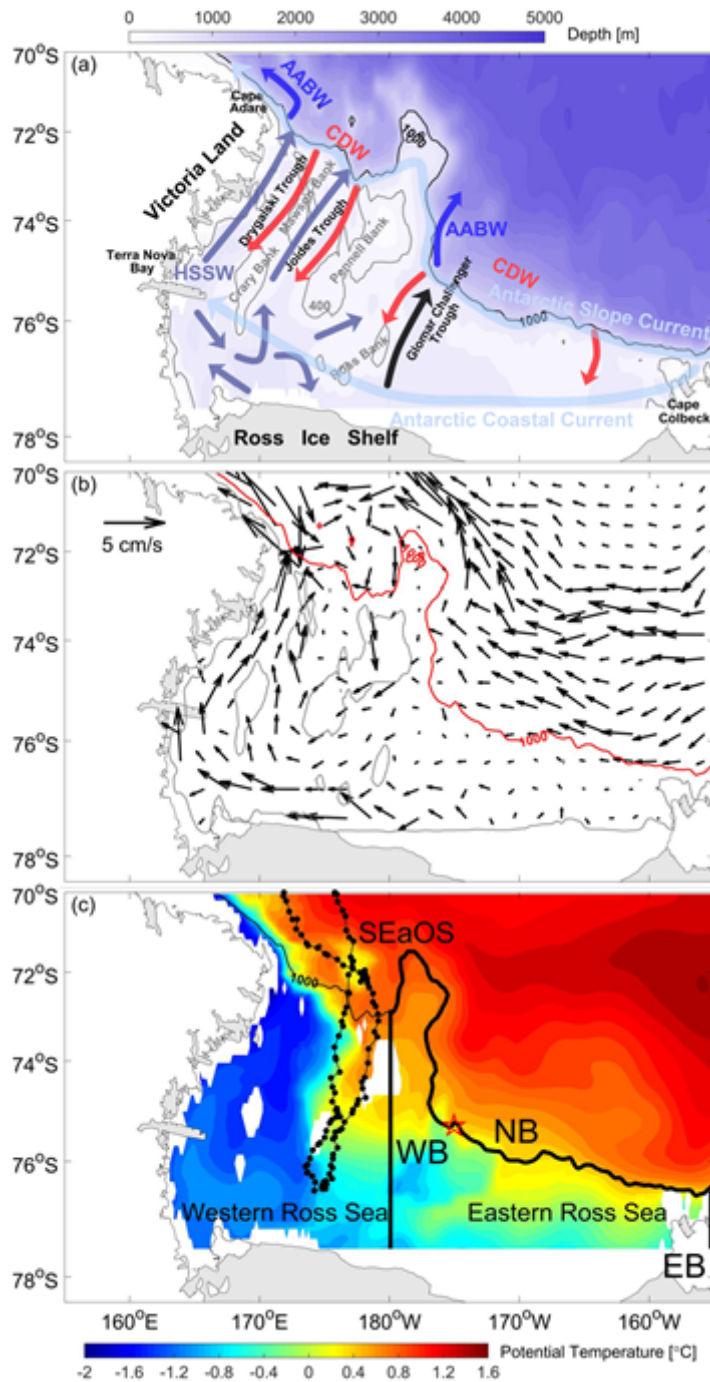


**Figure 1**

(a) The Ross Sea bathymetry (m). The gray and black lines represent the 400-m and 1000-m isobaths. The arrows show the schematic of major currents and horizontal pathways of water masses, including the Antarctic Slope Current, the Antarctic Coastal Current, the circumpolar deep water (CDW), the high salinity shelf water (HSSW), the Antarctic Bottom Water (AABW) and the Ice Shelf Water (ISW). (b) Currents at the depth of 328 m in 2005 from SOSE. (c) The average potential temperature at the depth of 328 m for 2005–2010. Open boundaries of the eastern Ross Sea shelf are indicated by the thick black lines. The seal trajectory from the SEaOS data is indicated by the black curve. The red star represents the

demarcation point between the western section and the eastern section of the northern boundary used in following analysis.

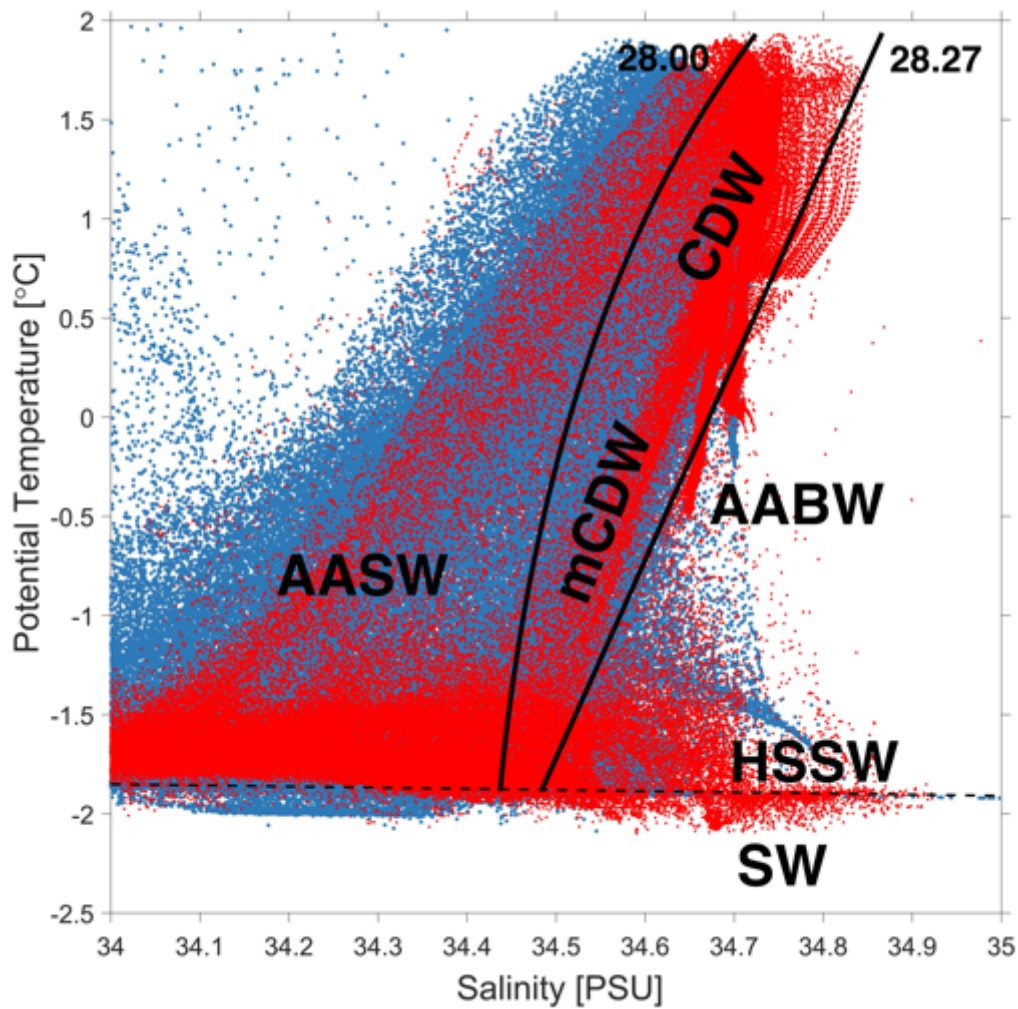


**Figure 2**

The temperature-salinity diagram from the SOSE data (blue dots) and the WOA18 data (red dots) in the Ross Sea. Solid lines show the neutral density ( $\gamma^n$ ) contours of 28.00 kg m<sup>-3</sup> and 28.27 kg m<sup>-3</sup>. The dotted horizontal line shows the surface freezing point of seawater. Major water masses are labeled: Antarctic Surface Water (AASW), circumpolar deep water (CDW), modified CDW (mCDW), Antarctic Bottom Water (AABW), High Salinity Shelf Water (HSSW), and Shelf Water (SW).

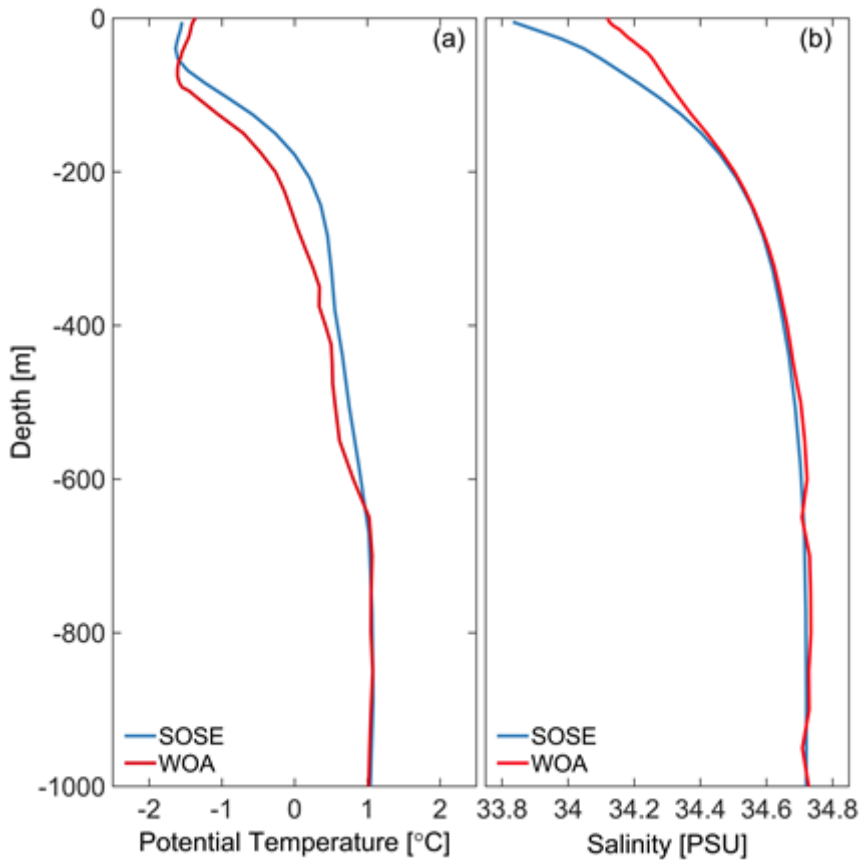


**Figure 3**

(a) Profiles of climatological potential temperature from SOSE (blue line) and WOA18 (red line) in the Ross Sea. (b) Profiles of climatological salinity from SOSE (blue line) and WOA18 (red line) in the Ross Sea.

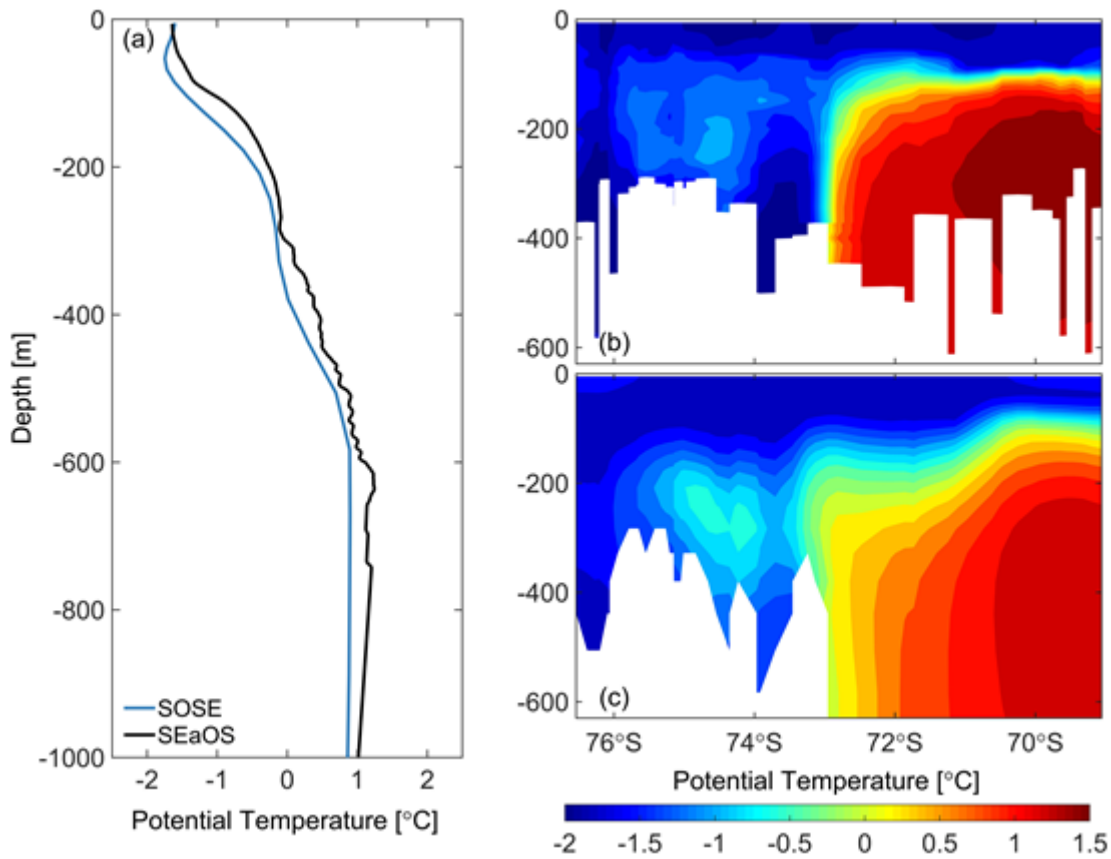


**Figure 4**

(a) Profiles of potential temperature from SEaOS (black line) and SOSE (blue line) averaged over the SEaOS section (indicated in Fig. 1c). Distributions of potential temperature from (b) SEaOS and (c) SOSE on the SEaOS section.

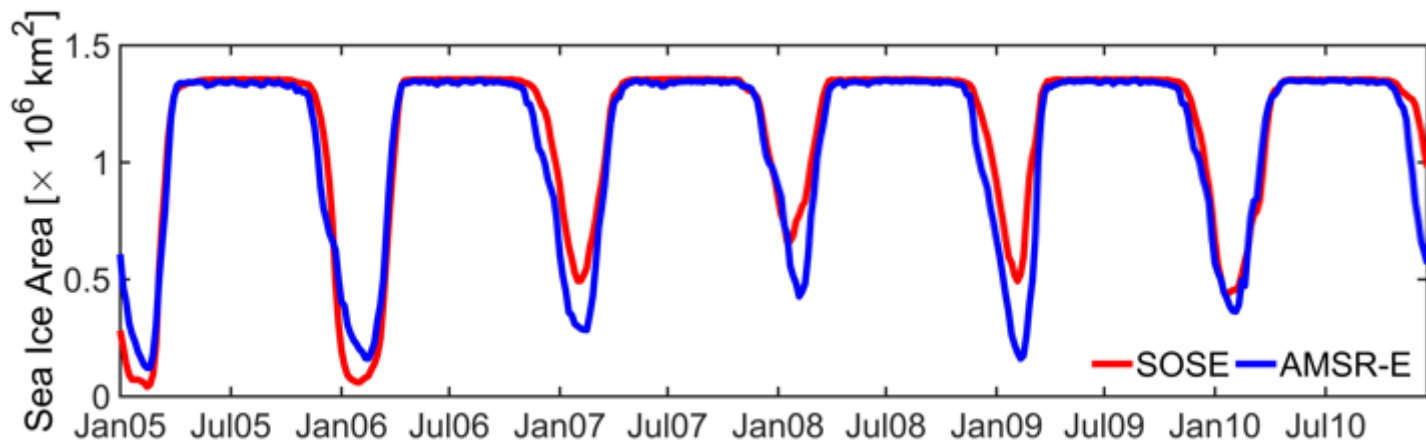


**Figure 5**

Temporal variations of sea ice area of SOSE (red line) and AMSR-E (blue line) from 2005 to 2010.

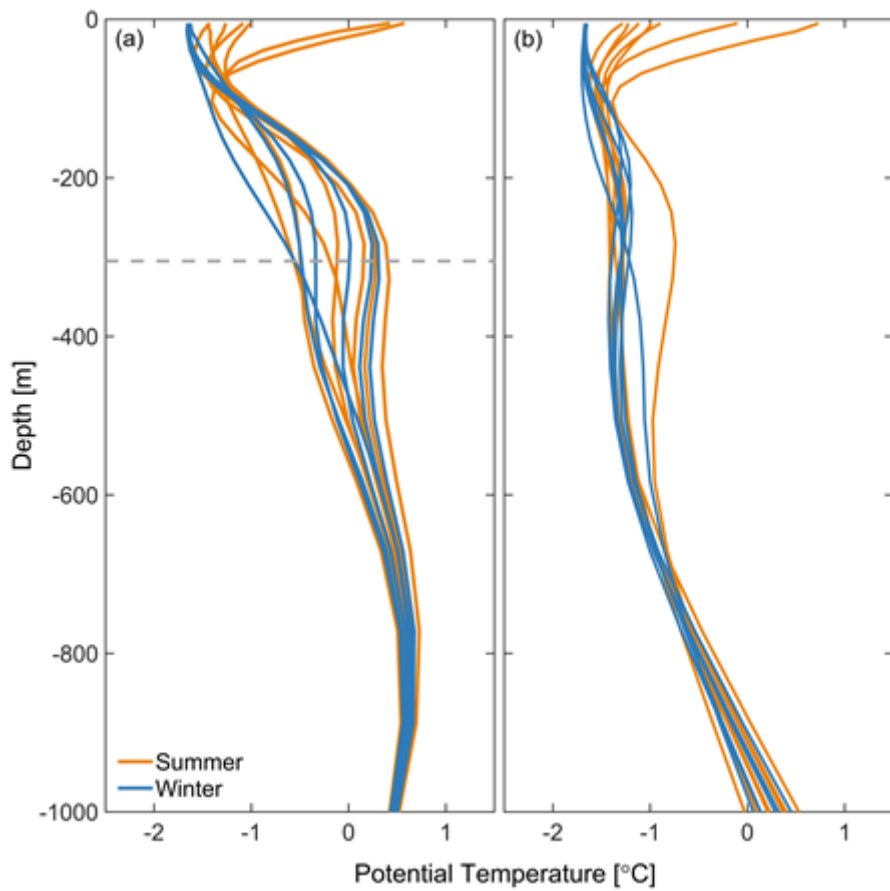


**Figure 6**

Profiles of austral summer (orange) and winter (blue) mean potential temperature from SOSE on the (a) eastern and (b) western Ross Sea shelf. Different lines in the same color indicate data from different years of 2005–2010. The gray dotted line in (a) represents the demarcation line between the surface layer and the subsurface layer in this study.

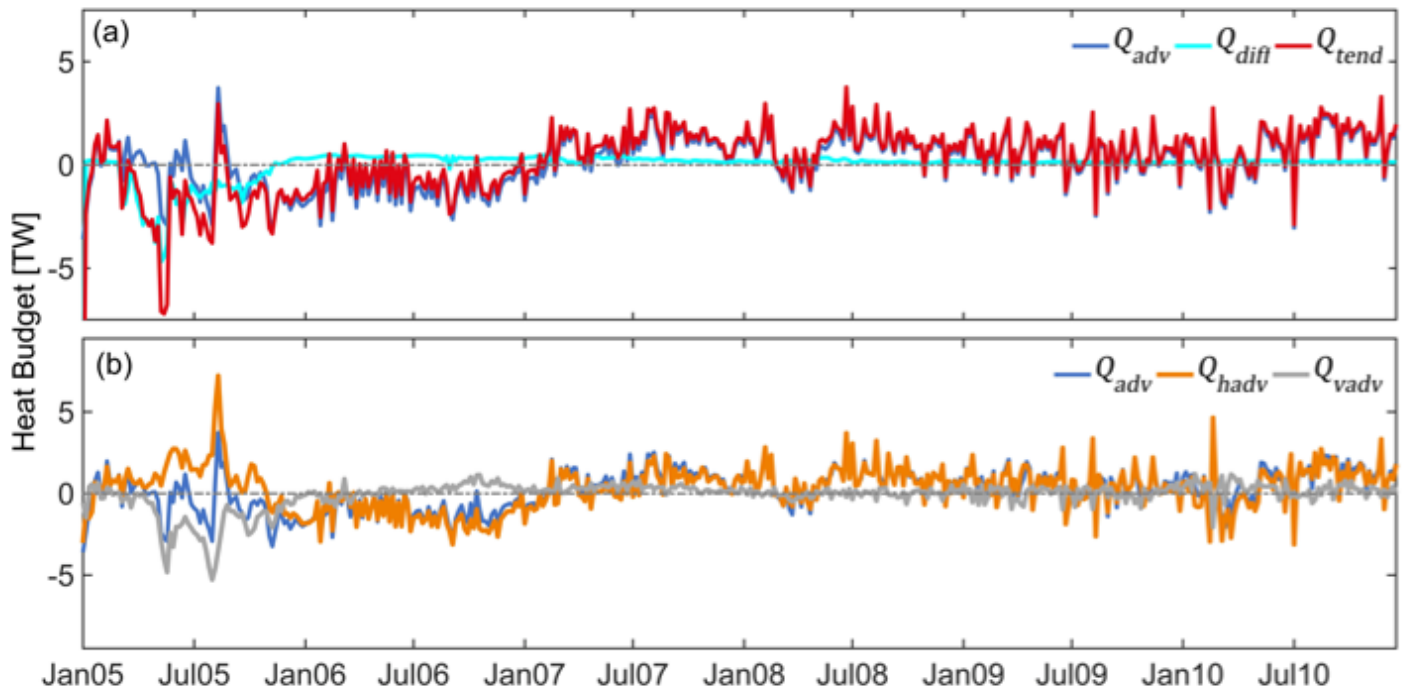


**Figure 7**

(a) Timeseries of the 5-day-average tendency term, advection term, and diffusion term in the heat budget equation for the subsurface layer of the eastern Ross Sea shelf. (b) Timeseries of the 5-day-average advection term, horizontal advection term, and vertical advection term in the heat budget equation.

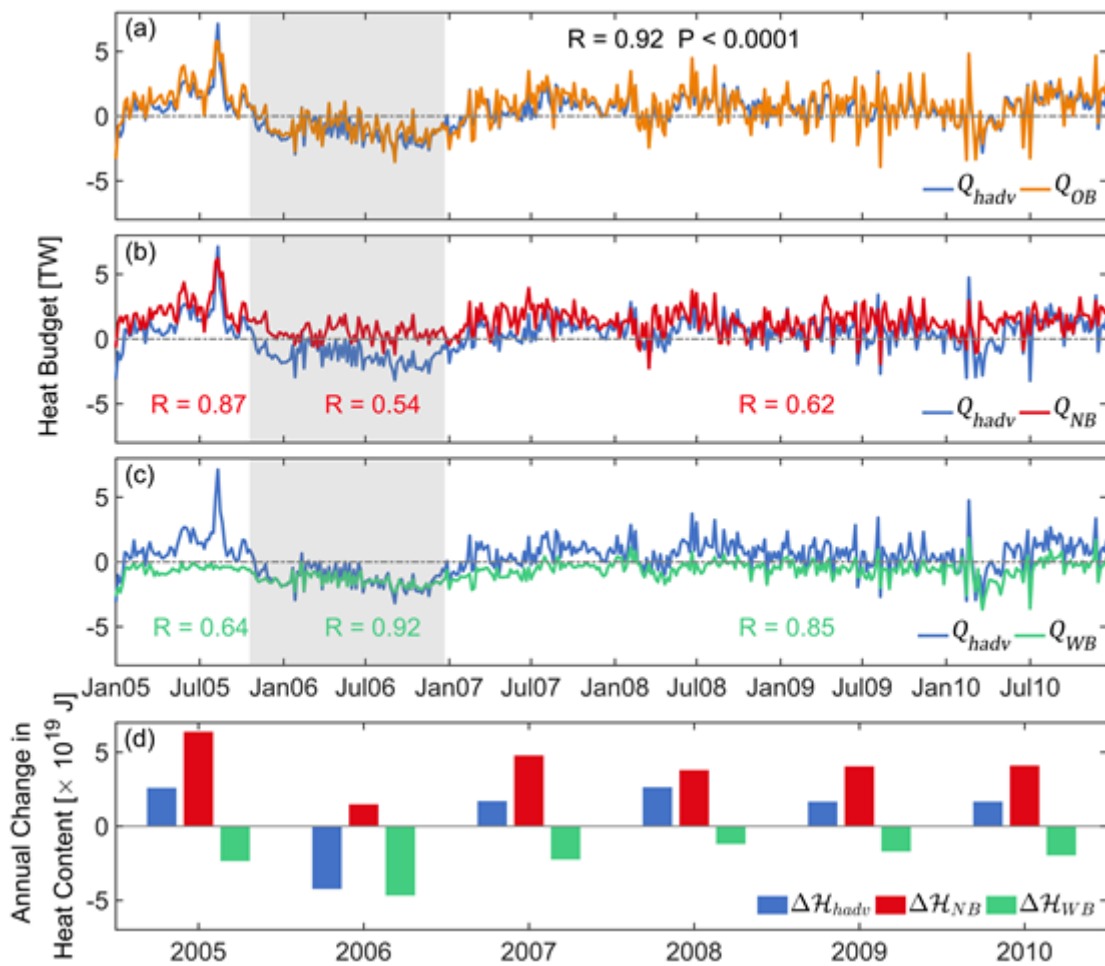


**Figure 8**

(a) Timeseries of the 5-day-average horizontal heat advection ( $Q_{hadv}$ ) and heat advection across the open boundaries ( $Q_{OB}$ ) of ERSS. (b) Timeseries of the 5-day-average heat advection across the northern boundary ( $Q_{NB}$ ). (c) Timeseries of the 5-day-average heat advection across the western boundary ( $Q_{WB}$ ). Correlation coefficients ( $R$ ) between the timeseries in (a)–(c) are indicated for different time periods. (d) Annual change of heat content related to the horizontal advection ( $\Delta\mathcal{H}_{hadv}$ ), advection across the northern boundary ( $\Delta\mathcal{H}_{NB}$ ) and advection across the western boundary ( $\Delta\mathcal{H}_{WB}$ ).

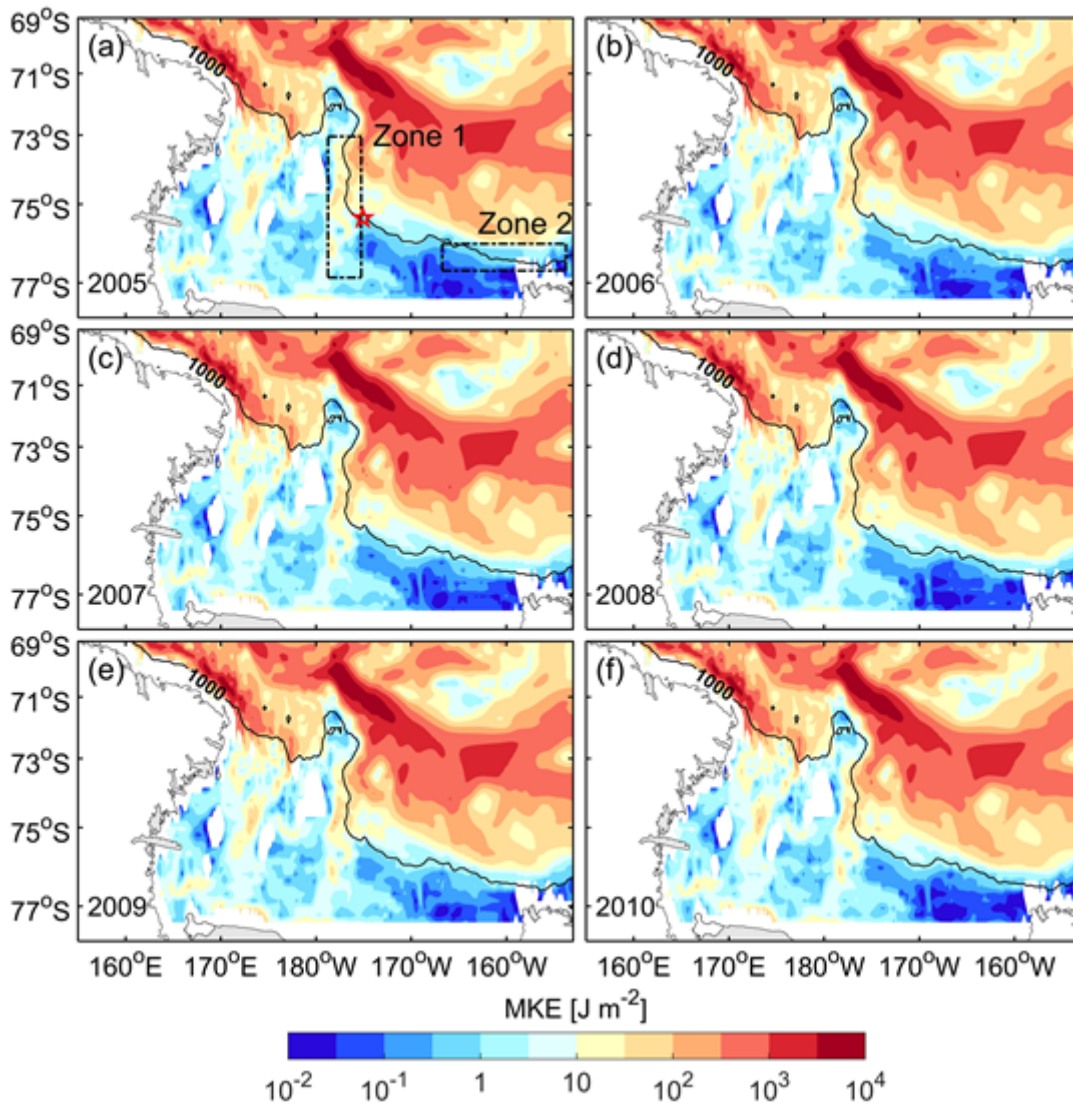


**Figure 9**

Distributions of annual-average vertically integrated MKE over the subsurface layer for 2005–2010. Zone 1 and Zone 2 are the areas characterized by strong CDW intrusion (Fig. 1a). The red star in (a) represents the demarcation point between the western section and eastern section of the northern boundary.

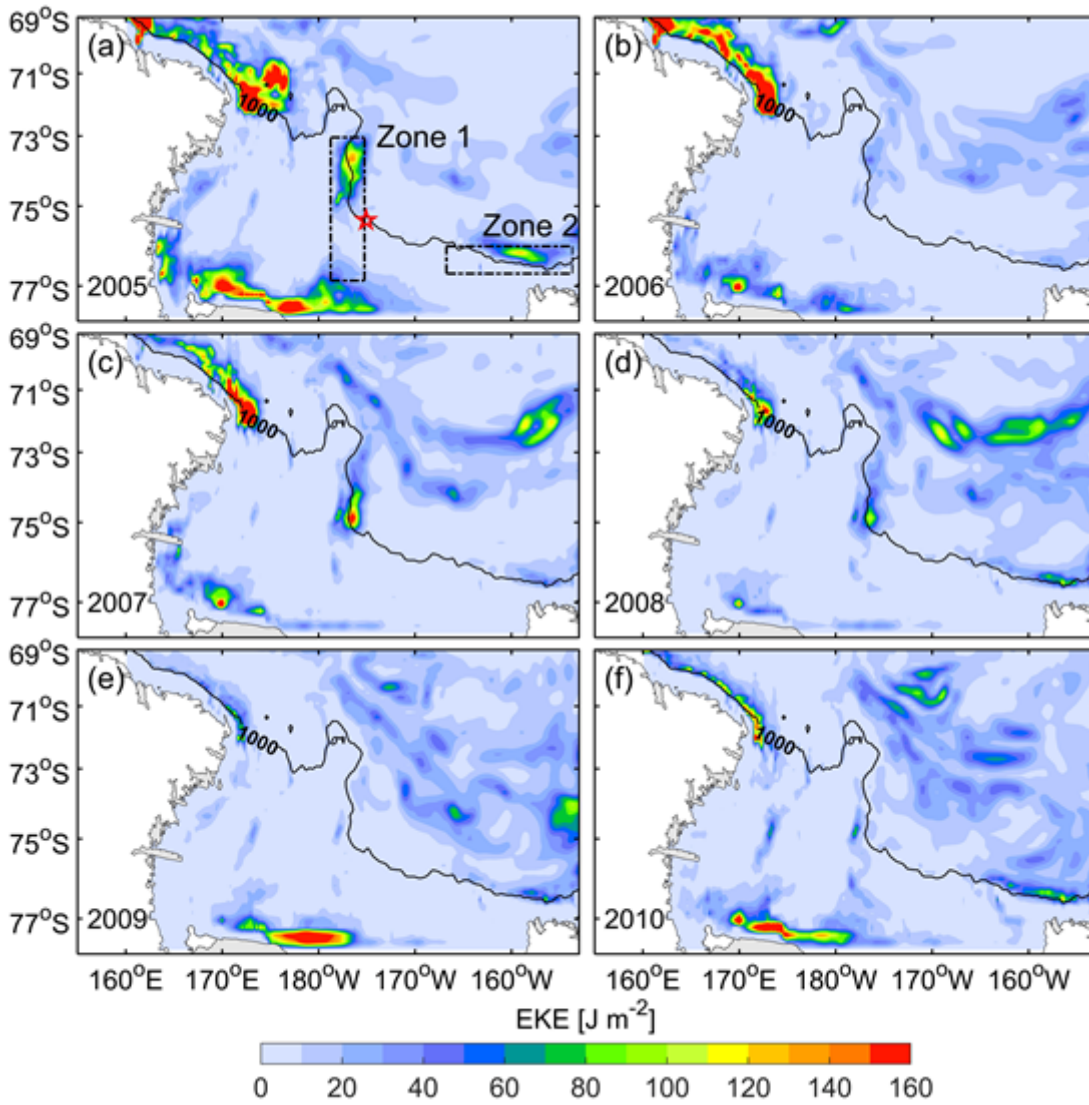


**Figure 10**

Distributions of annual-average vertically integrated EKE over the subsurface layer for 2005–2010. Zone 1, Zone 2, and the red star are the same as in Fig 9a.

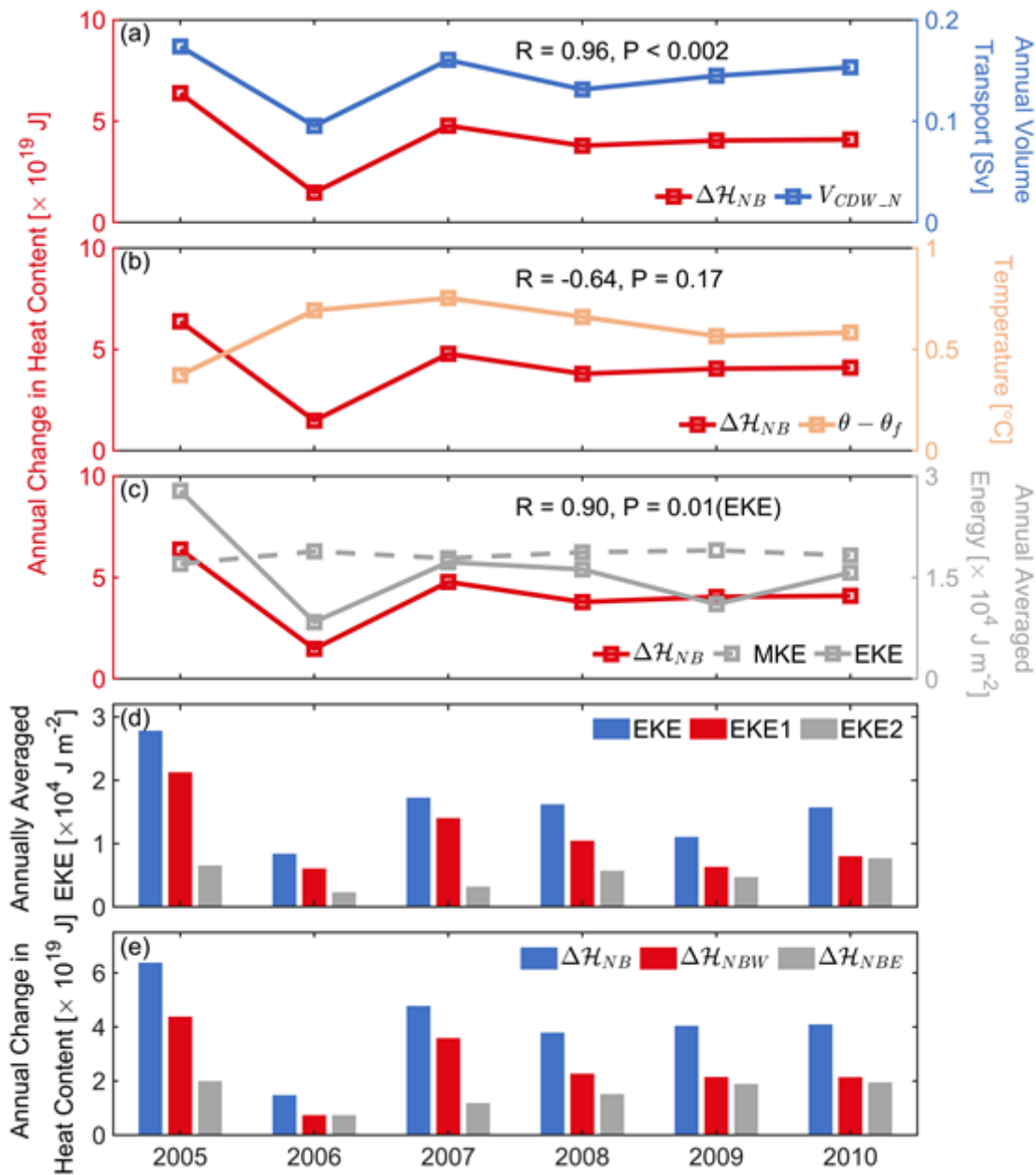


**Figure 11**

(a) Timeseries of  $\Delta H_{NB}$  and the annual volume transport of CDW ( $V_{CDW\_N}$ ). (b) Timeseries of  $\Delta H_{NB}$  and temperature difference between the northern boundary and the continental shelf ( $\theta - \theta_f$ ). (c) Timeseries of  $\Delta H_{NB}$ , the total MKE and the total EKE. (d) Annual values of EKE, EKE1 and EKE2. (e) Annual values of  $\Delta H_{NB}$ ,  $\Delta H_{NBW}$  and  $\Delta H_{NBE}$ .

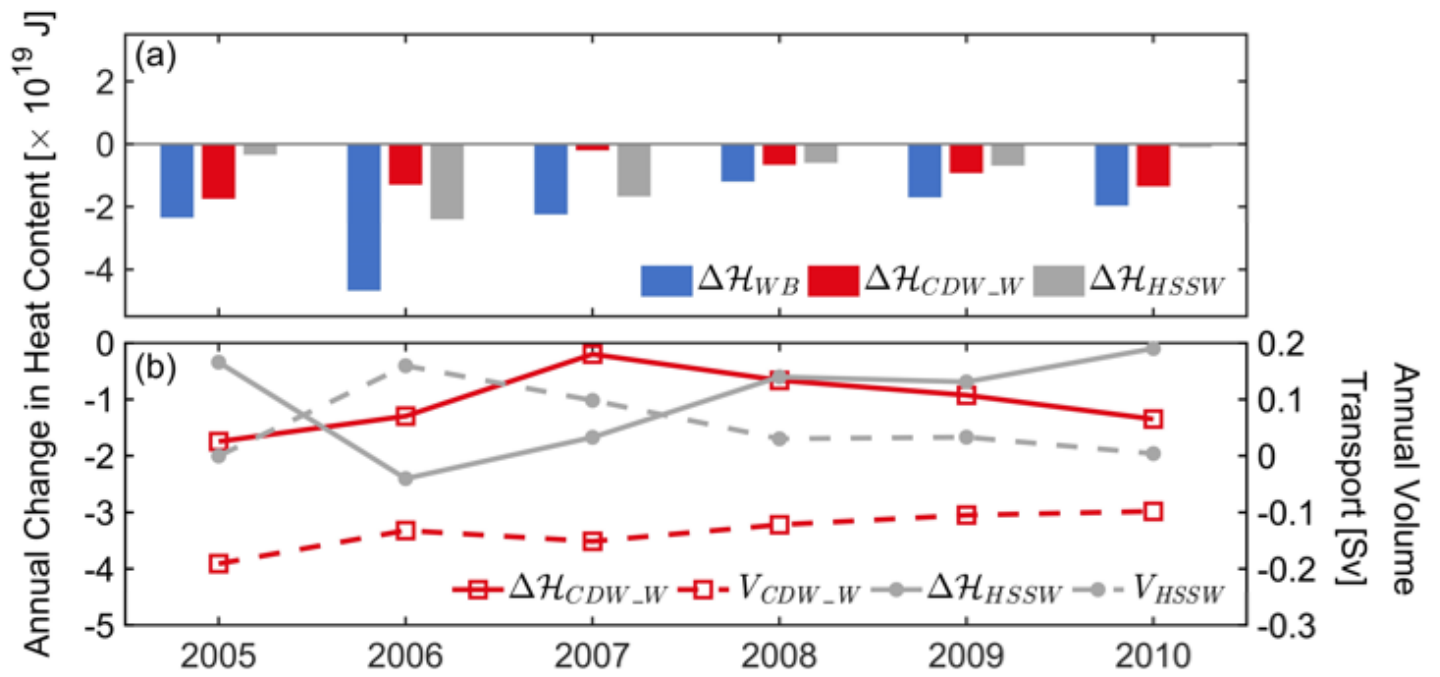
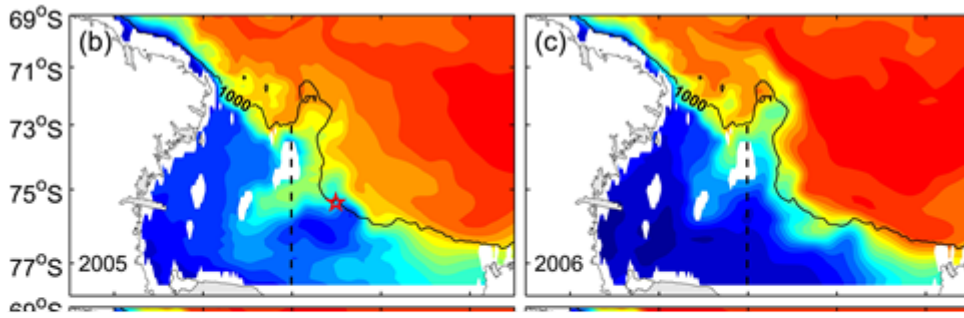


Figure 12

(a) Annual change of heat content related to  $Q_{WB}$  ( $\Delta\mathcal{H}_{WB}$ ),  $Q_{CDW}$  ( $\Delta\mathcal{H}_{CDW\_W}$ ), and  $Q_{HSSW}$  ( $\Delta\mathcal{H}_{HSSW}$ ). (b) Timeseries of  $\Delta\mathcal{H}_{CDW\_W}$ ,  $\Delta\mathcal{H}_{HSSW}$  and annual volume transport of CDW ( $V_{CDW\_W}$ ) and HSSW ( $V_{HSSW}$ ) across the western boundary.



**Figure 13**

(a) Annual change of heat content in the subsurface layer of ERSS ( $\Delta H$ ) for 2005–2010 associated with horizontal advection ( $\Delta H_{\text{hadv}}$ ), advection across the northern boundary ( $\Delta H_{\text{NB}}$ ), advection across the western boundary ( $\Delta H_{\text{WB}}$ ), advection due to the transport of CDW across the western boundary ( $\Delta H_{\text{CDW}_W}$ ), and advection due to the transport of HSSW across the western boundary ( $\Delta H_{\text{HSSW}}$ ). (b–g) Potential temperature at the depth of 328 m for 2005–2010. The black line is the 1000-m isobath. The red star in (b) is the same as in Fig 9a. The black dotted line in b–g represents the western boundary.

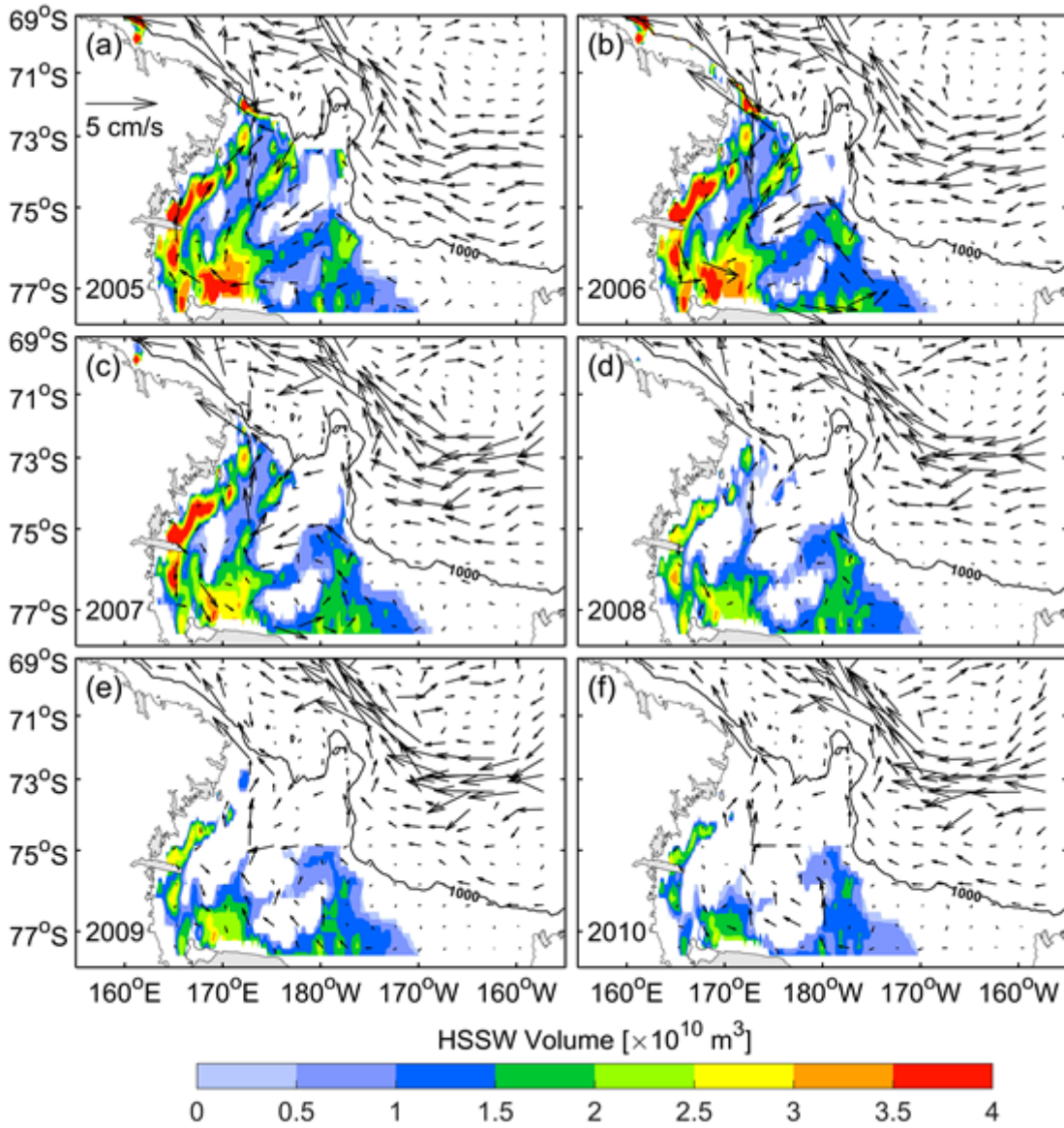


**Figure 14**

Distributions of the HSSW volume and vertically-averaged horizontal currents for the subsurface layer for 2005–2010 (a–f).

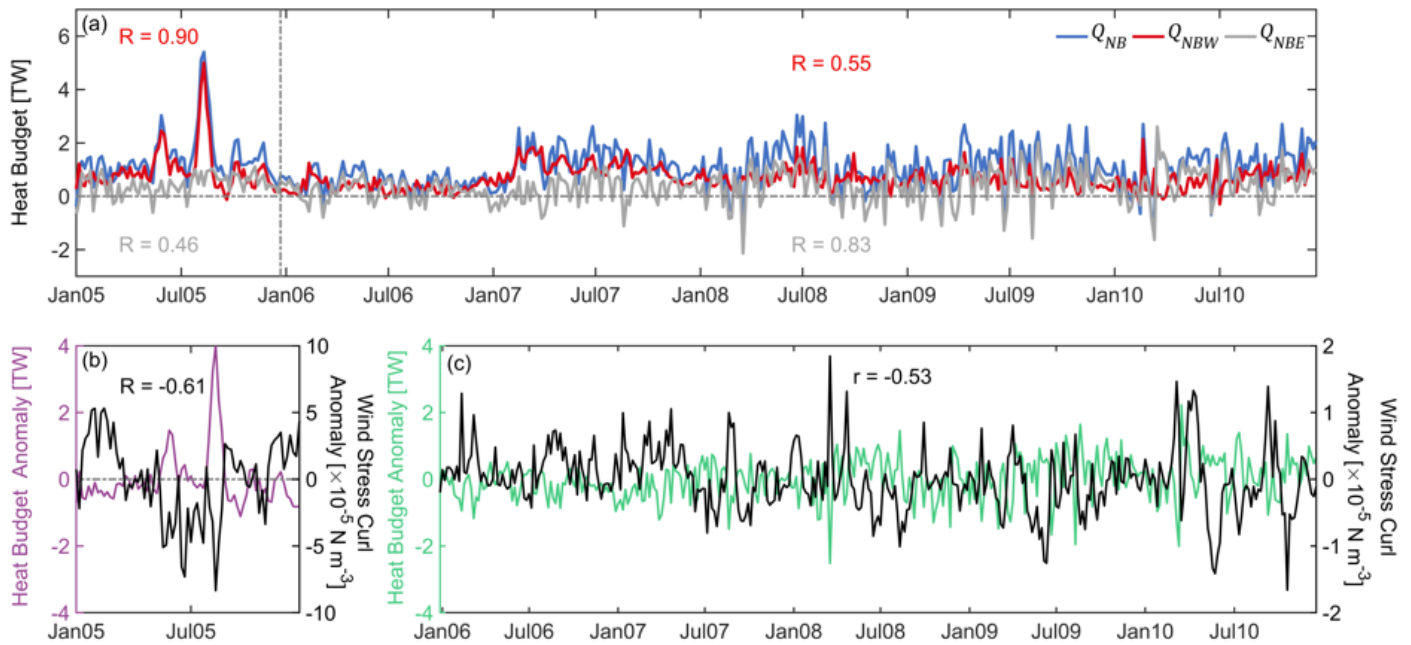


**Figure 15**

(a) Timeseries of the 5-day-average heat advection from the northern boundary ( $Q_{NB}$ ), the western section of the northern boundary ( $Q_{NBW}$ ), and the eastern section of the northern boundary ( $Q_{NBE}$ ). Correlation coefficients ( $R$ ) between  $Q_{NBW}$  and  $Q_{NB}$  (font in red color) and between  $Q_{NBE}$  and  $Q_{NB}$  (font in grey color) are indicated for different periods. (b) Timeseries of the  $Q_{NBW}$  anomaly (purple line) and the anomaly of wind stress curl averaged for areas offshore of the 1000-m isobath in Zone 1 (black line). (c) Timeseries of the  $Q_{NBE}$  anomaly (green line) and the anomaly of wind stress curl averaged for areas offshore of the 1000-m isobath in Zone 2 (black line). The correlation coefficient ( $R$ ) between the time series is indicated in (b) and (c) and all  $p$ -values ( $P$ ) are lower than 0.0001.